Sorting and provenance patterns in the Usumacinta-Grijalva delta, Mexico

---

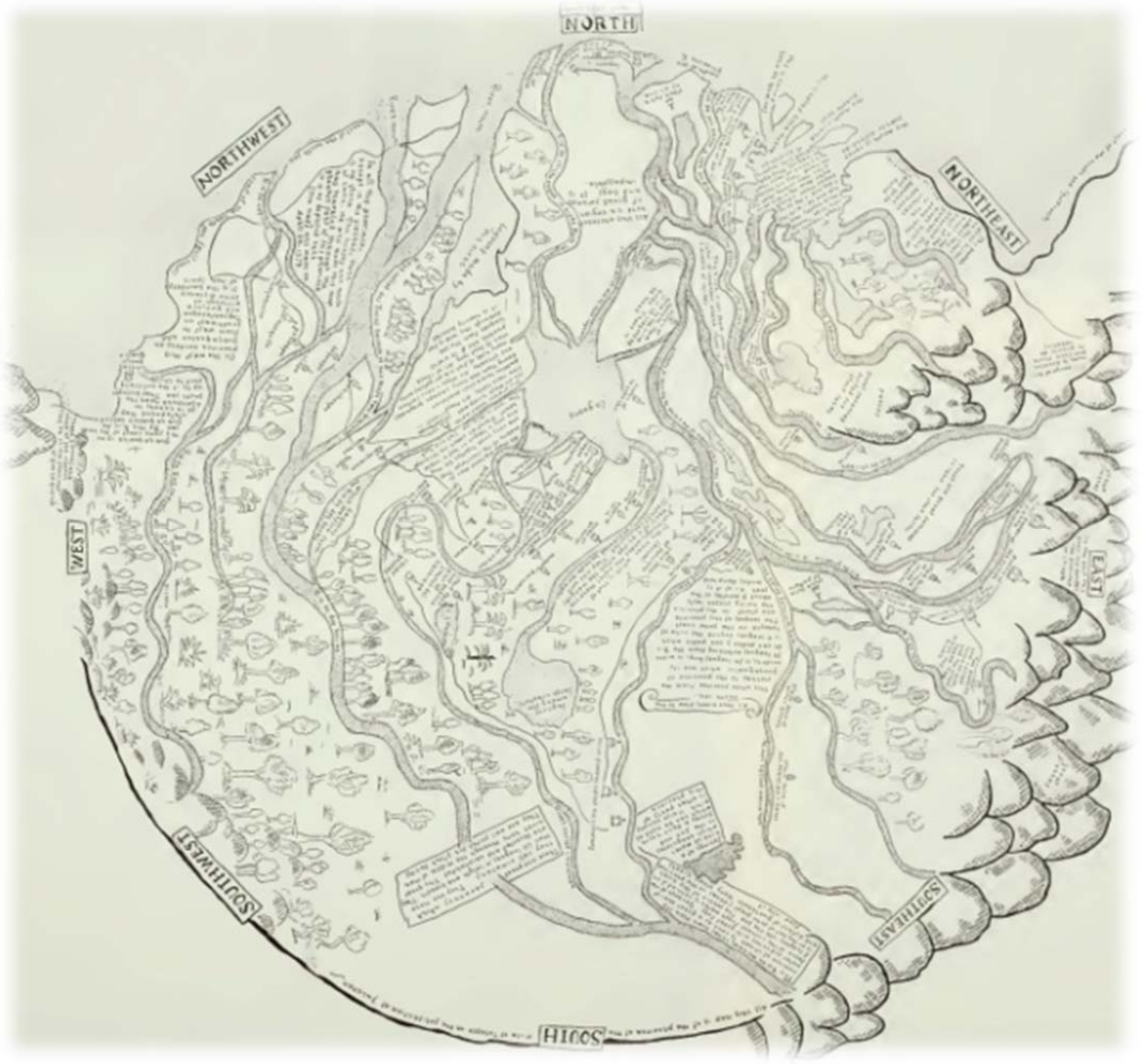

Master Thesis Earth Sciences
T.G.Winkels
Student number: 3245799
Utrecht University
Faculty of Geosciences
Department Physical Geography
Supervisor: W.Z. Hoek / C.A.M. Nooren

Abstract

The Usumacinta-Grijalva delta is located in southern Mexico and is characterized by the largest beach ridge plain in the world, with well over 500 consecutive beach ridges spanning roughly the last 5000 years. This beach ridge plain has the potential to be used as a high resolution paleo-environmental record since a sequence of beach ridges can be regarded as a time-series for coastal evolution. During the 2013 field campaign samples were taken from 70 different coring locations in a series of transects and additional corings covering the delta plain. For a selection (>200) of samples grain-size parameters were determined according to two different methods: sieving and laser-diffraction particle size analysis, while magnetic susceptibility was determined for all samples. End member modeling was performed on both grain size datasets, in order to unmix and quantify the relative abundance of different sediment populations. Based on provenance and sorting processes, a physical meaning has been assigned to each specific sediment population (end-member). Based on these labels, the contribution of the different river systems and coastal sorting processes, that play a role in the coastal evolution of the Usumacinta-Grijalva delta, were reconstructed. Using LIDAR images and sediment characteristics, five different phases of delta evolution could be identified.

Keywords *Beach ridges* *Grain size analysis* *Magnetic Susceptibility* *End-members*

T.G. Winkels
Faculty of Geosciences
Utrecht University
Department Physical Geography

Contents

T.G. Winkels
Faculty of Geosciences
Utrecht University
Department Physical Geography

T.G. Winkels
Faculty of Geosciences
Utrecht University
Department Physical Geography

List of figures

T.G. Winkels
Faculty of Geosciences
Utrecht University
Department Physical Geography

List of Tables

T.G. Winkels
Faculty of Geosciences
Utrecht University
Department Physical Geography

Acknowledgments

It has been almost over one year since I started working on this thesis. It was a long but fulfilling process that would not have been possible without the help of others. First of all I want to thank Wim Hoek for his assistance during the whole project and for showing me that doing good research does not imply researching everything. For me this is one of the biggest lessons I could have learned during this whole project! Furthermore I want to thank Maarten Prins for his help with the end-member modeling. I also want to thank Jesse James Hennekam for his assistance during the field campaign. Last but certainly not least I want to thank Kees Nooren for his continued help throughout the whole project. I enjoined the multiple brainstorm sessions we had about different aspects of the project!

T.G. Winkels
Faculty of Geosciences
Utrecht University
Department Physical Geography

1. Introduction

Since the start of the deglaciation the eustatic sea level started to rise. In the Holocene, the decrease in eustatic sea level rise resulted in the start of progradation of different deltas around the world. Deltas are generally classified based on the dominating building process; fluvial-dominated, tide-dominated or wave-dominated (Galloway, 1975). In wave-dominated deltas, diffusion and deceleration of river outflow by waves may eventually lead to the development of multiple beach ridges. Beach ridges are landforms which develop in propagation of coastal regions and are formed parallel or subparallel to the shoreline (Stapor, 1975). As beach propagation continues, beach ridges are cut-off from active coastal processes and preserved. These preserved beach ridges contain a complex record of different Holocene (climate) forcings; e.g. storm surge activity (Komar, 1998; Nott et al., 2009), sea level variations (Clemmensen et al., 2010; Tamura et al., 2008), and sediment supply/provenance (Brooke et al., 2008; Nott et al., 2013; Pontee et al., 2004; Rhodes et all., 1980). These factors determine beach ridge characteristics such as ridge morphology (e.g. ridge height; spacing) and internal structure (e.g. texture; mineralogy). Beach ridge complexes develop in various settings around the world (Fig. 1), under different processes (Tamura, 2012). Therefore, a sequence of beach ridges can be regarded as a time series of coastal evolution (Tamura, 2012), with a maximum resolution that corresponds with the average time interval of a single beach ridge. This average time interval is determined by dividing the total time span, of the beach ridge complex by the total amount of beach ridges. Investigation of multiple beach ridge complexes (~50) shows that on average, time intervals lies between 30-60 years (Tanner, 1995), thus showing the potential of beach ridge complexes as high resolution paleo-environmental records.

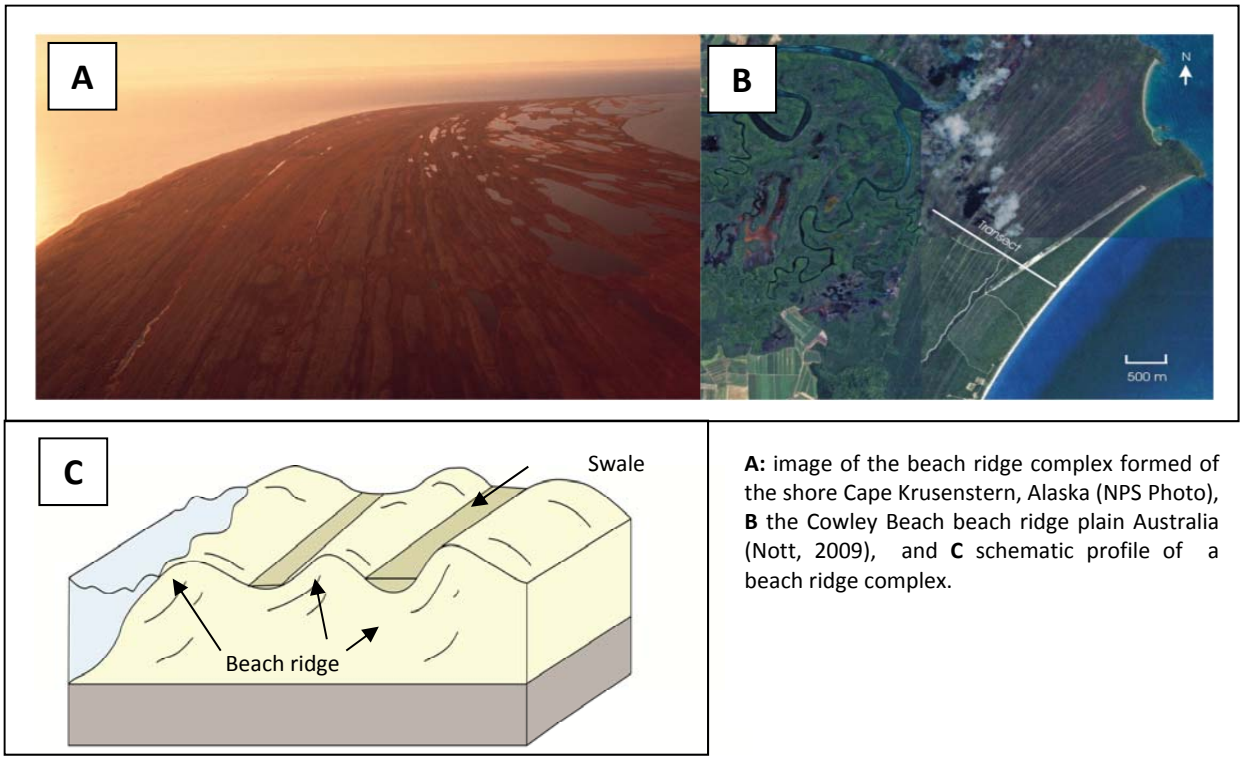

A: image of the beach ridge complex formed of the shore Cape Krusenstern, Alaska (NPS Photo), **B** the Cowley Beach beach ridge plain Australia (Nott, 2009), and **C** schematic profile of a beach ridge complex.

T.G. Winkels
Faculty of Geosciences
Utrecht University
Department Physical Geography

1.1 Aim of research

The goal of this study is to reconstruct sediment supply and sediment provenance in the Usumacinta-Grijalva delta. This is done by investigating sediments from multiple cores taken throughout the study area. The following research questions have been formulated:

1) Do the individual beach ridges show characteristic sorting patterns?
2) Is it possible to determine variations in sediment supply based on sorting patterns and heavy mineral content?
3) Is it possible to unravel mixing patterns in the different beach ridges and determine sediment provenance?
4) Is it possible to reconstruct different phases of delta progradation?

This study uses the term beach ridge deposits as deposits that were deposited by marine processes. Aeolian dunes sediment is always mentioned explicitly.

1.2 Thesis Outline

In chapter 2, a short overview of previous research is given. Multiple theories on beach ridges formation in relation to coastal processes are discussed, as well as an introduction of the implementation of heavy minerals in determining sediment provenance. Chapter 3 gives an overview of the regional settings of the study area including, climate, fluvial, geological and geographical characteristics.
In chapter 4, the approach of this research and used methods is set out. Chapter 5 gives the results of the research.
Chapter 6 presents the paleogeographic evolution of the Usumacinta-Grijalva delta. In Chapter 7 the result of this study are discussed and the approach of this research in compared to other beach ridges studies. The main conclusions are presented in chapter 8 while chapter 9 gives suggestions for future research.

T.G. Winkels
Faculty of Geosciences
Utrecht University
Department Physical Geography

2. Previous Research

In order to use beach ridge deposits as a paleo-environmental record, a basic understanding of their internal structure and composition is needed. Sediment characteristics, such as grain size distributions and mineral composition, are partly determined by this internal structure.

2.1 Beach Ridges

Beach ridge systems form a record of sediments transported to the coastal plain resulting in coastal progradation. Coastal progradation is, however, not a constant process, but is interrupted by phases of coastal erosion (e.g. storms changes in sediments supply). Examination of various beach ridge systems around the world shows different internal structures for individual beach ridges. Most common are landward dipping laminations (Fig. 2A/B, Carter, 1986; Psuty, 1965; Hine, 1979), but seaward dipping laminations are also identified (Fig. C/D/E, Carter, 1986; Tanner and Stapor, 1971). These internal laminations can be used to get insight in the genesis of the individual beach ridges. Multiple theories exist for beach ridges formation: storm built ridges, aeolian built ridges, swash bar "melting", and ridges build by sea level oscillation (Tamura, 2012).

Storm built ridges Multiple studies (Komar, 1998; Tamura, 2012; Taylor et al., 1996) propose storm waves as a mechanism for the building of beach ridges (Fig. 2A). During (high energy) storm conditions gravel sediments are transported up the beach slope. Due to the large porosity of these sediments, wave energy is dampened and back-wash currents are no longer able to transport these gravel sediments back to sea. This process of beach accretion eventually leads to the formation of a (storm) berm crest. Storm waves are thus proposed as main building mechanism for *gravelly beach ridges* (Taylor and Stone, 1996) with beach ridge height directly related to storm intensity. There is, however, no general consensus over the specific (grain size) boundaries for this kind of beach ridge formation.

Aeolian built ridges In contrast to storm built beach ridges another theory for the formation of sandy beach ridges involves aeolian processes during calm weather conditions (Fig. 2B/C). Several authors (Bird, 1960; Davies, 1957; Hail, 1969) argue that a berm nucleus forms the base for beach ridge development and that vegetation growing on these berm nuclei enhances the trapping of aeolian sediments and thus further build-up of the beach ridge. The presence of this so called berm nucleus does also require the occurrence of a storm. However, Hesp (1984) showed that vegetation development just outside the swash limit was enough to trap aeolian sediments, resulting in the build-up of a beach ridge.

Swash bar melting Another method for beach ridge formation is the melting of so called swash bars (Fig. 2D). When sufficient sand is transported to an offshore bar it can slowly built to sea level. This transport of sand can occur by means of two different mechanism: longshore and/or offshore transport (Curray et al., 1969). During periods with both low energy

T.G. Winkels
Faculty of Geosciences
Utrecht University
Department Physical Geography

wave conditions and high spring tides, these offshore bars can build up above the mean sea level. This process can repeat itself and eventually, unless high energy wave conditions erode the bar, a new beach ridge is formed. Anthony (2009) suggested that this mode of beach-ridge formation is relativity rare and is associated in regions where sediment supply is abundant, a low-gradient shoreface exists, and longshore currents are present.

Sea level oscillations Tanner (1995) proposed sea level changes as the basic mechanism behind the formation of beach ridges in low-energy sandy coast. He argued that due to multi-decadal changes in sea level and thus swash level, beach ridges of different height with a multi-decadal period can be formed (Fig. 2E). His findings are, however, questioned by Curuy (1996) and Otvos (1999). They question the presence of a multi-decadal oscillation in sea level and the absence of foredunes. Sea level oscillations as mechanism for beach ridge formation can, at present, not be verified or falsified and it is thus best not exclusively adopt this method for paleo-environmental reconstruction (Tamura, 2012).

Beach ridges systems have the potential to be used for paleo-environmental reconstruction. However, using beach ridge systems for paleo-environmental reconstruction requires consideration of certain restrictions and valid assumptions on genesis processes (Tamura, 2012). Without careful consideration of these limitations, beach ridges systems cannot be used for paleo-environmental reconstruction.

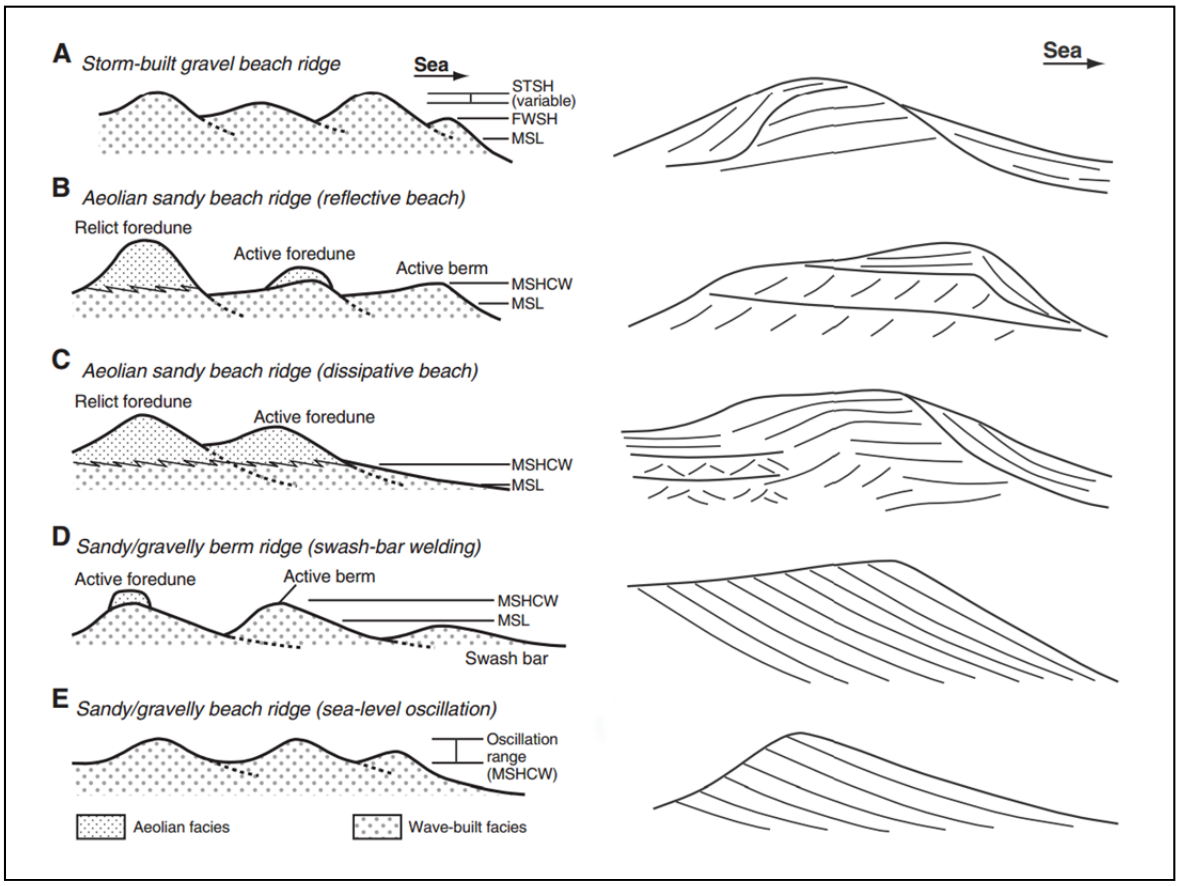

Figure 2: Proposed processes of beach-ridge formation and corresponding variations of internal sedimentary structures. MSL = mean sea level; FWSH = fair-weather wave swash height; STSH = storm wave swash height; SHCW = maximum swash height of constructive wave (After Tamura, 2012).

T.G. Winkels
Faculty of Geosciences
Utrecht University
Department Physical Geography

2.2 Heavy minerals

Coastal deltas contain large amounts of sediments, transported there by river(s) and reworked by coastal processes before eventually being deposited. The composition of these sediments depends on multiple factors such as source rock, reworking processes and post-depositional dissolution (Mange and Maurer, 1992). Especially heavy minerals are characteristics for determining the provenance of the sediment in coastal regions.

2.2.1 Hydrodynamic processes

Because of their relation with specific source areas, heavy minerals have been used as a proxy for sediment provenance and coastal progradation history since the mid-19th century. However, basic knowledge is needed about the processes which ultimately determine the amount of heavy minerals found in coastal deposits. An important aspect determining heavy minerals sorting patterns along coasts is the response of heavy minerals to the different hydrodynamic processes.

The original heavy mineral signal is determined by the type of source rock eroded (Garzanti et all., 2007). However, this signal is not similar to the signal measured in coastal sediments. Due to different hydrodynamic processes, during river transport and coastal reworking, this signal is altered. When looking at hydrodynamic behavior, heavy minerals have totally different properties compared to lighter minerals (Komar, 2007). There are three main characteristics that determine the hydrodynamic behaviour of a sediment grain; density, size and shape. Heavy minerals (ρ_{grain}>2.8 g/cm^3) show, in relation to the lighter minerals, a large range in grain densities within the most common heavy mineral group (Komar, 2007). The influence of these heavy minerals, although present in smaller quantities, is thus an important factor influencing sediment sorting patterns. Besides density, grain-size and shape also influence hydrodynamic behaviour of individual grains.

Examination of source rocks reveals that heavy minerals tend to have similar grain-sizes compared to other minerals (Feniaks, 1944; Kretz, 1966). However, this size ratio changes significantly when looking at minerals found in coastal deposits. Here heavy minerals tend to be significantly smaller compared to the average grain-sizes.

Another important process determining heavy mineral concentrations in coastal sediments is coastal erosion. A shift from beach accretion to beach erosion can result in selective displacement of certain (lighter) grains (Frihy et all., 2008) resulting in lag deposits with relatively high concentrations of heavy minerals.

2.2.2 Sediment Provenance

As mentioned earlier the original heavy mineral signal is determined by the type of source rock eroded (i.e. sediment provenance). Multiple studies exist where heavy minerals are used as a proxy for sediments provenance (e.g. Cascalho et all., 2007; Bateman et al., 2007; Garzanti et al., 2007). As the river flows through the landscape it picks up sediments which contain the heavy mineral signal of the local bedrock. Differences in bedrock are thus reflected in the

T.G. Winkels
Faculty of Geosciences
Utrecht University
Department Physical Geography

heavy mineral composition of sediments. Besides the composition, other characteristics such as mineral weathering / shape can also differ between regions, due to local erosion of older deposits.

2.2.3 Post-depositional processes

The heavy mineral composition found in deposits do not necessarily correspond with original composition. This is the results of post-depositional weathering which causes selective dissolution of certain heavy minerals. This leads to a change in ratio between certain minerals and/or total disappearance of certain heavy minerals (Van Loon et al., 2007). Not all heavy minerals are equally sensitive to these weathering processes (Table 1). Post-depositional weathering also affects the optical characteristics of heavy minerals (e.g. colors become less clear; extinction angle becomes less clear) making it more difficult to distinguish between the different minerals.

Table 1: Relative stability of detrital heavy minerals during burial conditions (After Morton et al., 2007)

Least stable	
↑	Olivine
↕	Pyroxene
↕	Calcic Amphibole / Andalusite / Sillimanite
↕	Epidote
↕	Titanite
↕	Kyanite
↕	Sodic Amphibole
↕	Staurolite
↕	Allanite
↕	Granet / Chloritoid
↕	Tourmaline / Monazite / Spinel
↓	Rutile / Anatase / Brooktie / Zircon / Apatite
Most stable	

T.G. Winkels
Faculty of Geosciences
Utrecht University
Department Physical Geography

3. Regional setting

During the Holocene, the Usumacinta and the Grijalva river built-up a large delta in the bay of Campeche (Nooren et al., 2009). This delta is characterized as one of the largest beach ridge plains in the world, with well over 500 consecutive beach ridges spanning roughly the last 5000 years. Looking at the Usumacinta-Grijalva delta the coast parallel beach ridges in combination with a strong coastal progradation near the river mouth, indicate a combination of a fluvial and wave dominated system. This dominant fluvial component means that river systems are an important/dominant source of sediments used for beach ridge formation. Rivers channels are however not fixed in the delta plain. River meandering cause's small scale changes in river position, while avulsions can lead to large scale relocation of river channels. These shifts in channel location inherently cause shifts in sediment delivery, thus affecting local beach ridge formation and delta progradation. The effect they have on delta progradation is inherent to the scale of the channels relocation. Large scale relocations result in large scale changes in sediment supply throughout the delta. Increased river channel discharge can also lead to local an increase in sediment delivery. Due to the fact that Grijalva and the Usumacinta have multiple branches discharging into the sea, changes in discharge distribution between these different channels can also influence sediment distribution throughout the delta.

3.1 Climate setting

Multiple metrological observation centers are present throughout Tabasco and surrounding provinces (Servicio Meteorológico Nacional). These observations centers have been collecting basic temperature and precipitation data since 1951 (Fig. 3).

Throughout the entire region, mean monthly temperatures stay relatively high during the entire year. Minimum temperatures are reached during January (approximately 23 ^{o}C) and maximum temperatures during May (approximately 29 ^{o}C). Mean annual precipitation values vary greatly by region, with 992 millimeters at the Tuxtla Gutierrez observation center and 3420 millimeters at the Teapa observation center. Although absolute precipitation values differ, annual patterns are similar throughout region. The wettest months are June through October, with maximum precipitation occurring in the months September and October accounting for approximately 30% of the annual precipitation. The driest months are May and April which account for approximately 5% of the annual discharge.

During the winter months (October – February) the region is characterized by strong northern winds known as *Nortes* which drastically influence the general weather pattern in Tabasco. These *Nortes* occur approximately a dozen times during winter and corresponds with significant drops in temperatures, strong cold (Northern) winds and heavy rain showers. These winds are an important climatic factor as they drastically change the general weather/wave patterns (3.4 Coastal setting).

T.G. Winkels
Faculty of Geosciences
Utrecht University
Department Physical Geography

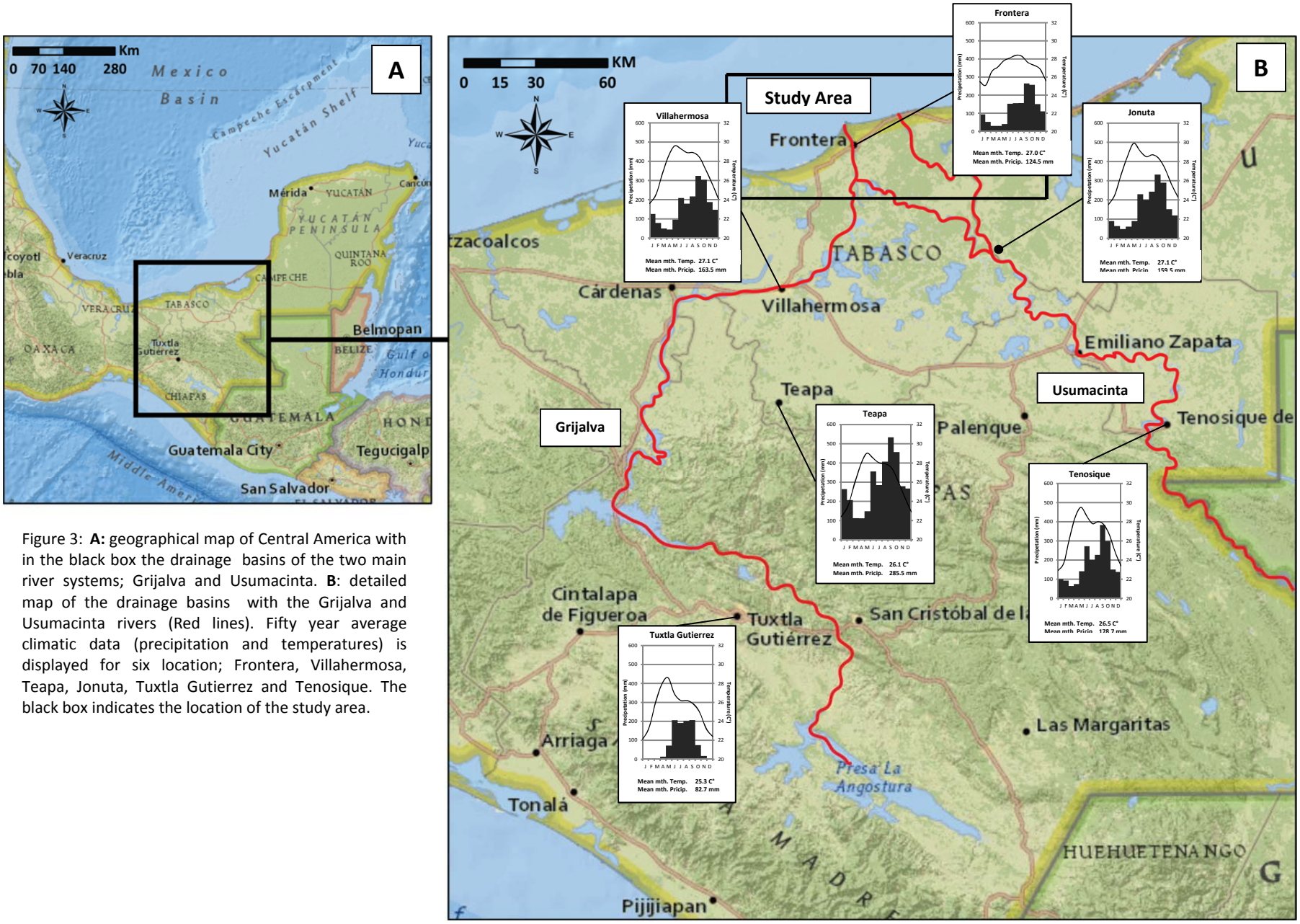

Figure 3: **A:** geographical map of Central America with in the black box the drainage basins of the two main river systems; Grijalva and Usumacinta. **B**: detailed map of the drainage basins with the Grijalva and Usumacinta rivers (Red lines). Fifty year average climatic data (precipitation and temperatures) is displayed for six location; Frontera, Villahermosa, Teapa, Jonuta, Tuxtla Gutierrez and Tenosique. The black box indicates the location of the study area.

3.2 Geological setting

Investigation of the geological setting in the two drainage basins reveals some major differences: towards the east the large carbonate platform of the Yucatan peninsula stretches further south, almost completely dominating the drainage basin of the Usumacinta. More towards the south west large scale igneous rocks are present in the Maya highlands where the Grijalva finds its origin (Fig. 4).

Another important geological factor is the El Chichón volcano which is situated within the drainage basins of the Grijalva and has a violent eruption character. Each eruption results in about 2km^3 of sediments into the drainage basin, leaving large area covered with volcanic ash after an eruption. Espíndola et al (2000) identified 12 explosive eruptions of the El Chichón volcano, occurring at approximately 550, 900, 1250, 1500, 1600, 1900, 2000, 2500, 3100, 3700 and 7700 years BP (Nooren et al., 2009).

3.3 Fluvial systems

The study area is located in Tabasco in the southern part of Mexico (Fig. 3). It is dominated by two main river systems; the Usumacinta and the Grijalva. In the northern part of Guatemala the *Pasión* and the *Salinas* river convulse to form the Usumacinta. From here the Usumacinta flows north defining for a large part the border between Guatemala and Mexico. Near the town *Tenosique de Pino Suárez* the Usumacinta enters the lower plains of Tabasco, here the rivers sinuosity increases significantly. Eventually the near the town of *Palizada* the old main channel of the Usumacinta (still active) flows north while the present day main channel flows towards the west eventually convulsing with the Grijalva near the town of *Tres Brazos* before draining into the Gulf of Mexico. The entire draining basin of the Usumacinta stretches approximately 64,400 km^2.

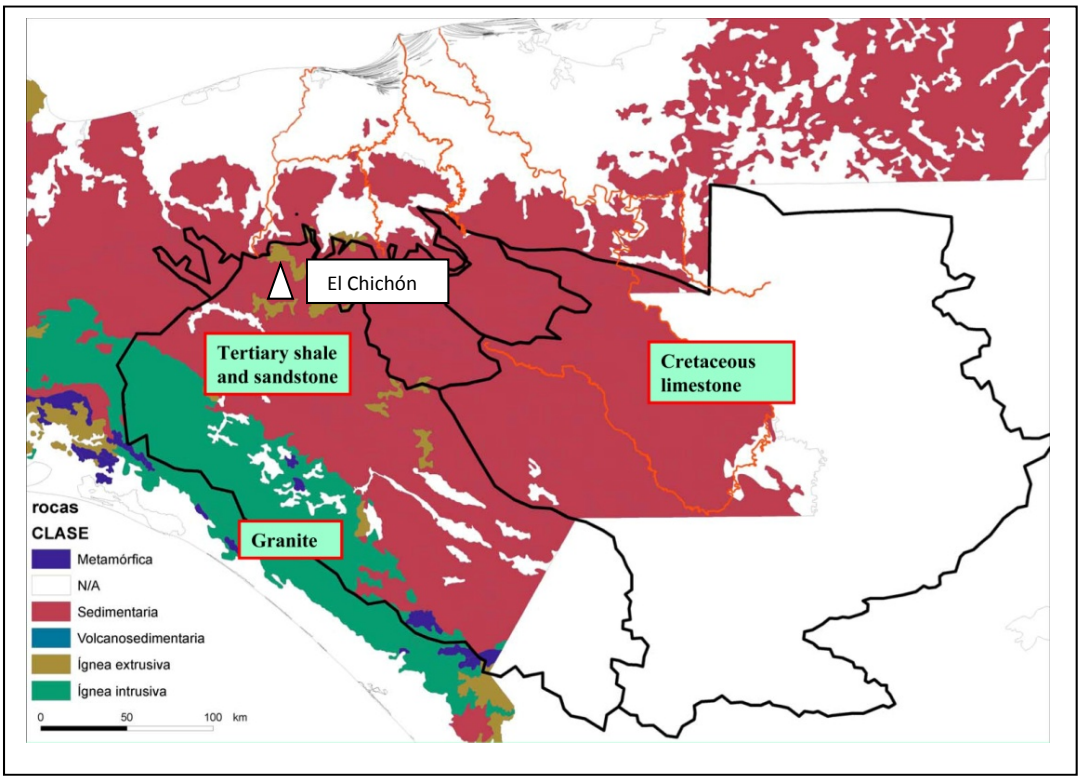

Figure 4: Geological map of Guatemala and Mexico showing the large carbonate platform of the Yucatan peninsula towards the south east and a large granite body in the south western part of Guatemala..

Mean annual discharges for the Usumacinta, measured between 1963-1985 at *Boca del Cerro*, lies around 1650 m^3/s. The other main river system, the Grijalva, originates in the south-western part of Guatemala and flow north into Mexico. At present, near the town of *Cárdenas,* the river course shift towards the east. Towards the north is the now abandoned *Rio Seco* which in the past was an important branch of the Grijalva. Near Villahermosa, the *Sierra River* merges with the Grijalva. The entire draining basin of the Grijalva stretches approximately 36,600 km^2. Mean annual discharges for the Grijalva lie around 1000 m^3/s. However, differences in monthly precipitation are also evident in rivers discharges, with peak discharges exceeding 9000 m^3/s for the Grijalva and 6500 m^3/s for the Usumacinta, during the wettest months. At present the Usumacinta has a meandering flow pattern along its entire river course while the upstream Grijalva is characterized as a braided river system while more downstream it shows a meandering flow pattern

3.4 Coastal setting

Coastal settings vary on different timescales. On a long timescale, coastal settings are dominated by global sea level fluctuations. While on a short timescale, tides and wave action become the dominant processes. Global sea levels changes are the result of changes in ocean volume and can directly be correlated to changes in ice storage and/or thermal expansion/contraction (e.g. Engelhart et al., 2009). Since the onset of the deglaciation, global sea levels started to rise, reaching their maximum around 5000 yr. BP. Due to the lack of a locally constructed sea level curve, the sea level curve constructed for Belize (Gischlera et al., 2004) was used as a substitute (Appendix 1A). For shorter timescales the tidal and wave settings become important. The southern Gulf of Mexico is characterized by a micro tidal regime, with tidal amplitude ranging between 0.35-0.65 m (Appendix 1B). Waves have an average annual height of 1.2 meters (NOAA, Buoy 42055). However, during (*norte*) storms/hurricanes these values can increase significantly.

3.5 Anthropogenic impact

The Usumacinta-Grijalva delta shows a long record of different civilizations for more than 7000 years (Pohl et al., 2007; Pope et al., 2001). Deforestation and agricultural land drastically changed erosion patterns in both the delta as the hinterland possibly causing an increase in sediment supply to rivers and lakes. The last 100 years the civil population has increased significantly from approximately 120,000 in 1900 to the approximately 1.9 million people living in the state of Tabasco at present. Although population increased significantly, the Tabasco area is not an ideal settling location due to its sensitivity for floodings. To better regulate river discharges and thus floods, and for the generation of hydropower production, during the mid-20^{th} century five dames were constructed upstream in the Grijalva. However, the construction of these dams was not sufficient to protect the lower delta plains from flooding. This became clear during the floodings in 2007, which in inundated almost 80% of the state Tabasco. Beside regulating river discharges, these dams drastically alter sediment transport of the Grijalva creating an sediment deficient in regions behind these dams.

T.G. Winkels
Faculty of Geosciences
Utrecht University
Department Physical Geography

4. Methods

High resolution LIDAR images of the Usumacinta-Grijalva delta provide a detail survey of the entire study area. Using these LIDAR images, potential different stages of delta evolution were identified. In order to reconstructed changes in sediment composition for these different stages, cores were taken along three different transects each strategically chosen to incorporate different stage of delta progradation (Fig. 5).

4.1 Coring

During the fieldwork over 70 cores where taken along three different transects (Fig. 5). These transects, with varying resolutions. In addition to the drilling along transects, single cores were taken in remote areas. Coring depth was on average around five meters below surface; in some locations cores were taken up to eleven meters below surface. Depending on whether the coring was done above or below the groundwater table different coring techniques have been used. For coring above the groundwater table an Edelman corer was used, while for coring below groundwater a *Van der Staay* suction corer was used to retrieve sediments. Except for cores taken to investigate aeolian properties, all cores were taken from the lower situated swales. Cores for aeolian were sampled every 20cm while other cores were sampled every 50cm. All samples were taken back to the Netherlands for sedimentary analysis.

4.2 Ground penetrating radar (GPR)

Ground penetrating radar (GPR) measurements were performed during the field campaign of 2012 by *R. van Dam*. GPR is a method for high-resolution imaging and mapping of subsurface layers. The principle behind GPR is as followed: a short high-frequency electromagnetic pulse is sent into the ground. This pulse is scattered back towards the surface where a receiver picks up the scattered signal. This scatter pattern depends on the electrical properties of the subsurface material and can thus be used for imaging of subsurface. An more detailed description of this method and applied processing methods, performed by R. van Dam, can be found in Appendix 2.

4.3 Grain size

This study uses grain size analyses to reconstructed changes in sediment composition and eventually supply. Over 800 samples were collected during the field campaign of 2013, from over 70 different locations. Grain-size parameters were determined according to two different methods: sieving and laser-diffraction particle size analysis. It was not the goal of this study to make a full comparison between these two methods; hence they should be interpreted as two independent proxies.

4.3.1 Sieving analysis

The sieve defines a particle diameter as the length of the side of a square hole through which the particle can just pass. Generally samples are pretreated by removing organic and

T.G. Winkels
Faculty of Geosciences
Utrecht University
Department Physical Geography

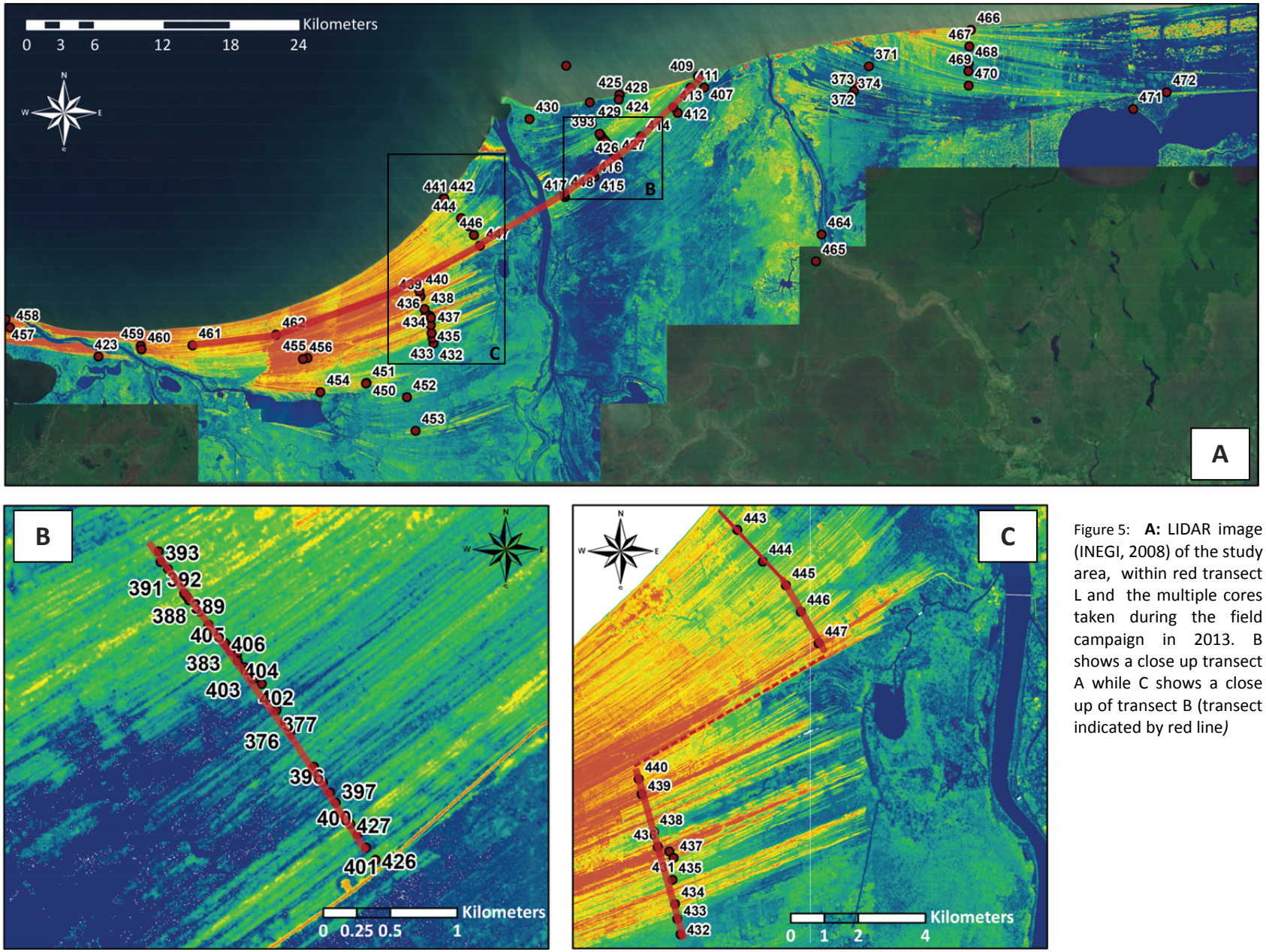

Figure 5: **A:** LIDAR image (INEGI, 2008) of the study area, within red transect L and the multiple cores taken during the field campaign in 2013. B shows a close up transect A while C shows a close up of transect B (transect indicated by red line*)*

carbonate content (NEN 5753), to prevent flocculation. Previous research in this region however showed that organic/carbonated content of beach ridge sands, except for samples with large amounts of carbonated shells and the organic layers, is low. The percentage of carbonate shells is therefore visually estimated and corrected for. To save time, samples were not pretreated. All samples were dried before sieving using a set of twelve consecutive sieves, ranging between 26 -500 µm (Appendix 3).
Grain-size analysis was done along the different transects. Due to time restriction not all samples were analyzed. A selection was made based on exploratory work done on five consecutive cores (Cores: 375-379). For these cores, grain size distributions were determined every 50cm. Examination of these grain-size distributions revealed that samples taken at 150cm, 300cm and 500cm depth below surface level best represent distribution variability throughout the entire core. In some specific cases sample depth had to be corrected for "extreme swale height". This was done by using the groundwater table as reference height instead of surface level.

4.3.2 Laser-diffraction analysis

Based on the sieving results, a selection of samples was made which showed 1) significant variation in grain-size distributions along transects or 2) overall deviating grain-size distributions. Grain-size analysis following Konert et al. (1997) was performed at the VU Faculty of Earth and Life Sciences Amsterdam. Laser diffraction grain-size analysis is based on the principle of light diffraction. Before samples are measured, organic matter and carbonates have been removed while certain ions like Ca2+, Fe3+ must be extracted. All samples were boiled in a *20% H_2O_2* solution which dissolved all the organic matter. Further treatment with *10% HCL* dissolved all carbonates. By washing the samples during the next step the ions are removed. Because some particles are electrically charged, these particles attract each other, making that they are interpreted as one big particle giving an incorrect grain size value. To eliminate these inconsistencies, ~300mg of *natriumpyrophosphate* has been added to the samples to separate the different particles from each other (peptization). During measuring the sample solution is continuously pumped around ensuring random orientation of most particles. The emitted laser beam is continuously diffracted by the different particles. Each diffraction angle corresponds with a specific particle size. Detectors measure the intensity of the diffracted light and, assuming a spherical particle shape, through a set of complex calculation calculated the grain-size distributions (Beuselinck et al., 1998). The Laser Particle Sizer has a measuring range which lies between 0.15-2000 µm. To cover the entire range, multiple focus lengths have been used. After a set of calculations the laser diffraction patterns are transformed into 57 grain size classes.

4.3.3 Grain-size statistics

Grain-size analysis is a powerful tool and can give insight into underlying processes of sorting. Grain-size parameters can provide clues to the transport history, provenance and/or depositional conditions of the sediment (Blott, 2001). To quickly calculate a range of grain-size parameters (e.g Mean, Mode, Sorting, Kurtosis) the program Gradistat is used (Blott, 2001).

T.G. Winkels
Faculty of Geosciences
Utrecht University
Department Physical Geography

This program uses different methods to calculate the various grain-size parameters for the sieve dataset. This study uses the method described by Folk and Ward (1957). Besides these general grain-size parameters, another form of grain-size analysis was applied; end-member modeling, which due to its complexity is discussed in detail in the next chapter.

4.4 End-Member Modeling

Grain-size distributions are composed of different sediment populations (Middleton, 1976; Bridge, 1981) and are the result of linear mixing processes such as (1) mixing of different sediment populations (e.g sediment provenance), and (2) selective mechanisms operating during transport and deposition (e.g. longshore sorting processes) (Prins, 1999). The objective of End Member modeling (EMM) is to unravel these different sediment populations, without any prior knowledge of the geological system.

When looking at sediments deposits, perfectly mixed sediments can be expressed as:

$$X = AS$$

where X represents the measured (sediment) dataset, A the mixing proportions of each individual sample and S the different end-members (Heslop, 2008). However, due to sampling/measurements errors, samples are never perfectly mixed and X can better be expressed as X = X' + E, where X' represents the ideal mixing system and E represents the error of the corresponding measurements Assuming these errors are relatively small and the non-negativity constraints of A (Prins and Weltje, 1999) sediment deposits can better be expressed by:

$$X = AS + E$$

Because no prior information is available, only X is known. The goal of EMM is to determine the unknowns A, S and E from X. A detailed review of how these unknown variables A, S and E are calculated is given by Heslop (2007) and Prins and Weltje (1999). Based on provenance and sorting processes, a physical meaning is eventually assigned to each specific sediment population (end-member).

EMM was done using the DRS-unmixer model (Heslop et all., 2007). In order to determine which end member model best explains the variations in the grain-size distributions, for each end member model the coefficients of determination of each individual grain-size class were calculated. Because the bulk of sediment is constrained to a specific grain-size range, and reproducibility of this grain-size range is important, these corresponding r^2 of this specific grain-size range was used to determine the goodness of fit of each specific end member model (Fig. 11). Generally speaking a higher number of end-members would result in higher r^2 values and thus a better unmixing model. This is, however, not entirely true for the DRS-unmixing model. In order to contribute a physical meaning to end-members have to be non-negative. However, the DRS-unmixer model only tests this requirement after calculating the multiple r^2 values by excluding certain data (negative grain-sizes) from the final EM calculation. Therefore higher order end member models sometimes have a lower r^2 value. Another disadvantage of

T.G. Winkels
Faculty of Geosciences
Utrecht University
Department Physical Geography

the DRS-unmixer model is that resulting end-members do not sum up to 100 percent. These deviations are, however, relatively small and can be easily corrected for by linearly stretching of the specific end-members (Appendix 4).

4.5 Heavy Minerals

Heavy mineral analyses can be used as a method for determining sediment provenance. Although this is not the focus of this study, the preliminary results can give insight in the practicality of this method in this specific area and may provide a basis for future research on this subject. In total, heavy mineral percentage was determined for 20 samples taken throughout the study area and upstream of the different river systems. A sub selection of five samples was made (2x Grijalva, 1x Usumacinta, 2x delta reference samples) for detailed heavy mineral determination. Besides hydrodynamic processes, aeolian processes can also alter sediments heavy mineral compositions. This post depositional sorting leads to a more complex heavy mineral signal. To avoid this, samples for heavy mineral analysis were taken only from beach ridge deposits and not from aeolian dunes. Assumed is that sediments deposited below the minimum (paleo) groundwater table were never able subjected to aeolian processes; hence all samples were taken under this minimum (paleo) groundwater table. Assuming minimum groundwater levels corresponds with sea level, paleo water levels are constructed using the sea level curve of Belize (Gischlera et al, 2004*)*. To correct for regional differences samples were taken 150 cm below the paleo water table (Appendix 5).

The percentage of heavy minerals found in sediments is grain-size related (Mange and Maurer, 1992). Therefore, a single/standard grain-size range (90-106µm) was chosen for heavy mineral analyses. Gravity separation was used to separate the light from the heavy minerals. Samples were added into a funnel containing a heavy liquid (Sodium Polytungstate - $Na6[H_2W_{12}O_{40}]$) with a density of 2.85g/cm^3. Due to gravity, the heavy minerals (density > 2.85g/cm^3) slowly accumulated in bottom of the funnel just above a pinch clip, while the lighter minerals float on top (Fig. 6). Once settling process is complete the pinch clip is slowly opened and the heavy mineral fraction is drained over an 8µm mesh sieve. After the heavy mineral fraction is collected, washed and dried, the magnetic minerals are extracted using a small magnet. Remaining minerals were mounted on a slide using the *glycerine* (*n=1.47*) and analyzed under polarization microscope (Mange and Maurer, 1992).

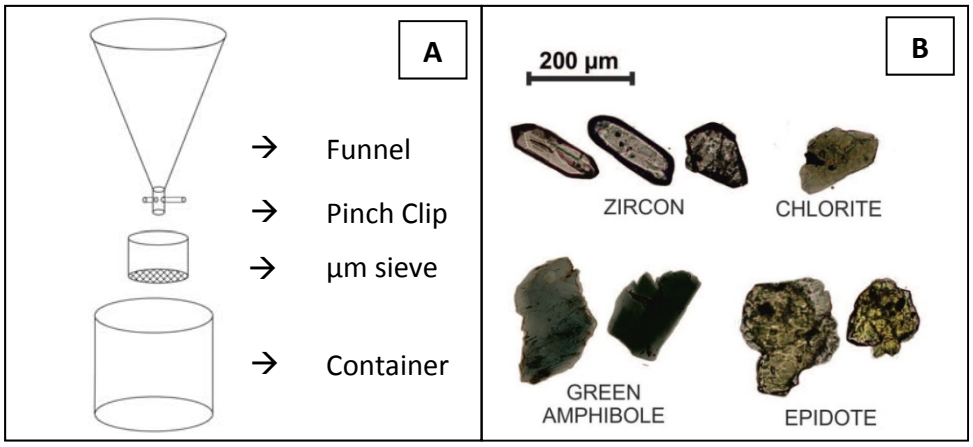

Figure 6: **A**: illustration of the setup used for extracting heavy minerals for sediments. B:an example of some heavy minerals found in beach ridge deposits(modified after Solis et al. 2013)

T.G. Winkels
Faculty of Geosciences
Utrecht University
Department Physical Geography

4.6 Magnetic Susceptibility

Magnetic susceptibility is an effective and fast method for determining the presence of certain (iron-bearing) minerals. Besides iron-bearing minerals, measurements are especially sensitive to specific minerals (Table 2). Magnetic susceptibility is a measure of the ease with which a particle is magnetized. With magnetic susceptibility analysis a sample is exposed to a small magnetic field, after which the magnetic signal is measured. Beside sediments composition, grain-size and shape also influence the magnetization of the samples and thus the magnetic susceptibility values.

During this study a *ZH instruments SM 30* was used to determine the magnetic susceptibility. Samples were placed on top of plastic container to prevent influence from metallic components. Because certain minerals have a much higher impact on the magnetic susceptibility signal when compared to other minerals, it is important to analyze the magnetic minerals and identify the specific minerals that can influence the magnetic susceptibility signal. Examination of samples reveled that all sediments samples contain varying amounts of magnetite. Due to the high impact factor of magnetite on the magnetic susceptibility values, this study assumes that the magnetic susceptibility directly reflects the amount of magnetite present in the sediments samples.

Table 2: Magnetic properties of certain minerals (After Schwertmann and Taylor, 1977)

Mineral	Formula	Magnetic Status	Magnetic Suceptibility *(10 -sm 3 kg 1)*
Hematite	ə Fe_2O_3	Canted antiferromagnetic	40
Goethite	əFeOOH	Canted antiferromagnetic	70
Ferrihydrite	$5Fe_2O_3$	Paramagnetic	40
Lepidocrocite	7FeOOH	Paramagnetic	70
Maghemite	Fe_2O_3	Ferrimagnetic	26000
Magnetite	Fe_3O_4	Ferrimagnetic	56500

4.7 Chronology

The potential for using beach ridges complexes as paleo-environmental record depends mainly on an accurate chronology. Without this, it is impossible to place the entire research into a timeframe and reconstruct delta evolution. Dating was done according to two different methods: *Optically Stimulated Luminescence and Radiocarbon dating*.

4.7.1 Optically Stimulated Luminescence dating

Optically Stimulated Luminescence (OSL) dating (e.g. Aitken, 1998; Wallinga, 2002) uses the luminescence signal trapped in sediments to derive the time since it was last exposed to sunlight. Natural radioactive particles continuously bombard sediments with α, β and γ particles. This leads to ionization of the surrounding materials which causes electrons to be trapped in light-sensitive traps within the crystal lattice of the quartz and feldspar minerals. Exposure to sunlight releases these trapped electrons, a processes called bleaching (Fig. 7). Once sediments are buried this luminescence signal can build up and thus be used to determine the time since a sample was last exposed to sunlight.

T.G. Winkels
Faculty of Geosciences
Utrecht University
Department Physical Geography

During the field campaigns of 2012 and 2013 multiple samples were taken for OSL dating. Samples were collected just below the water table in an non translucent PVC tube to prevent light exposure. The dating of the OSL samples was carried out by the Netherlands Centre for Luminescence dating (NCL) in *Wageningen*. Due to processing time, on average one year, only the samples that were collected during the 2012 field campaign are available (Appendix 6A).

4.7.2 Radiocarbon dating

Radiocarbon dating is a radiometric dating technique that uses the decay of ^{14}C to estimate the age of organic materials. Newly built organic tissue in living organisms incorporates the present atmospheric ratio between unstable ^{14}C and stable ^{12}C. Thus the carbon ratio within that organism will be in equilibrium with the surrounding atmosphere. This uptake of carbon stops when an organism dies, after which the ^{14}C starts to decay thus changing the $^{14}C/^{12}C$ ratio. An accelerator mass spectrometer directly measures the isotopic ratio between the unstable ^{14}C and stable ^{12}C. This ratio is then compared to a reference sample to obtain the amount of years since the specific organism died. However, due to the fact that the $^{14}C/^{12}C$ ratio in the biosphere is not constant, ^{14}C ages have to be calibrated using a calibration curve.

Organic material was collected from small debris layers, generally a few centimeters thick, within the beach ridge deposits. These debris layers contain large amounts of organic material. Reservoir age can pose a problem when dating small pieces of wood as they have a high preservation potential. However, leafe fragments have a very low preservation potential, and need to be deposited fast after its "death" in order to be preserved. Therefore, only leafe fragments were used for AMS ^{14}C dating. In total 21 samples were dated in the AMS facility in Groningen (van der Plicht et al., 2000). Calibration of samples was done using OxCal 4.2 and the resulting ^{14}C dates and calibrated age are shown in Appendix 6B.

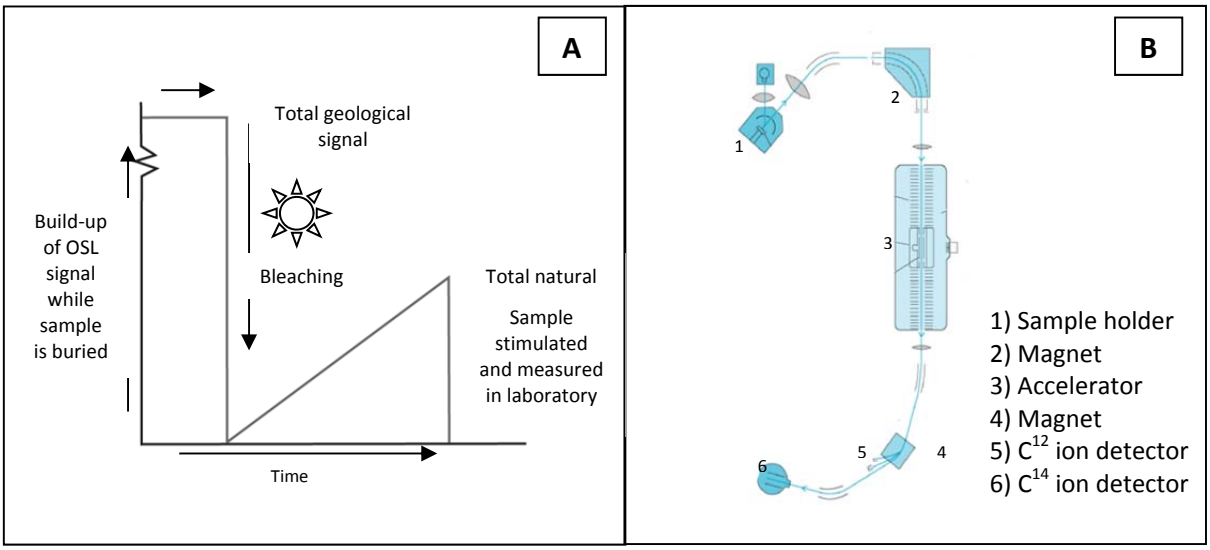

Figure 7: **A:** illustration of the accumulation and resetting (bleaching) of an OSL signal, modified after Minderhoud, 2011. **B** shows a simplified diagram of an accelerator mass spectrometer used for radiocarbon dating (American Heritage Dictionary).

T.G. Winkels
Faculty of Geosciences
Utrecht University
Department Physical Geography

5. Results

5.1 Internal structure

Although beach ridge formation as individual processes is not the scope of this research ground penetrating radar profiles measured during the 2012 field campaign gave an insight in the internal structure of the beach ridges (Fig. 8). Dimensions (i.e. depth) are not perfectly known due to the fact that propagation velocities were estimated.

Despite these uncertainties, this GPR profile (Fig. 8) does provide a preliminary insight in the internal structure of individual beach ridges. The upper unit (yellow in fig. 8)) shows a relatively horizontally deposited structure, which can be interpreted as aeolian dune deposits. Indicated by the blue lines, a few clear seaward dipping reflector layers can be recognized. Although this is no conclusive evidence for explaining beach ridge formation, it does show the potential of GPR for investigating internal structure, and thus formation history, of individual beach ridges.

5.2 Sediment analysis

To reconstructed changes in sediment composition and eventually supply within the delta, *grain-size parameters*, using Gradistat, and *magnetic susceptibility* values where analyzed along the three different transects (Fig. 9).

Transect A In the south a sudden increase in D_{50} values occurs simultaneously with a significant decrease in sorting and kurtosis values. This is followed by decrease in D_{50} values and small increase in sorting and kurtosis values. More towards the north D_{50} values gradually increase while kurtosis and sorting values are characterized by a gradual decrease.

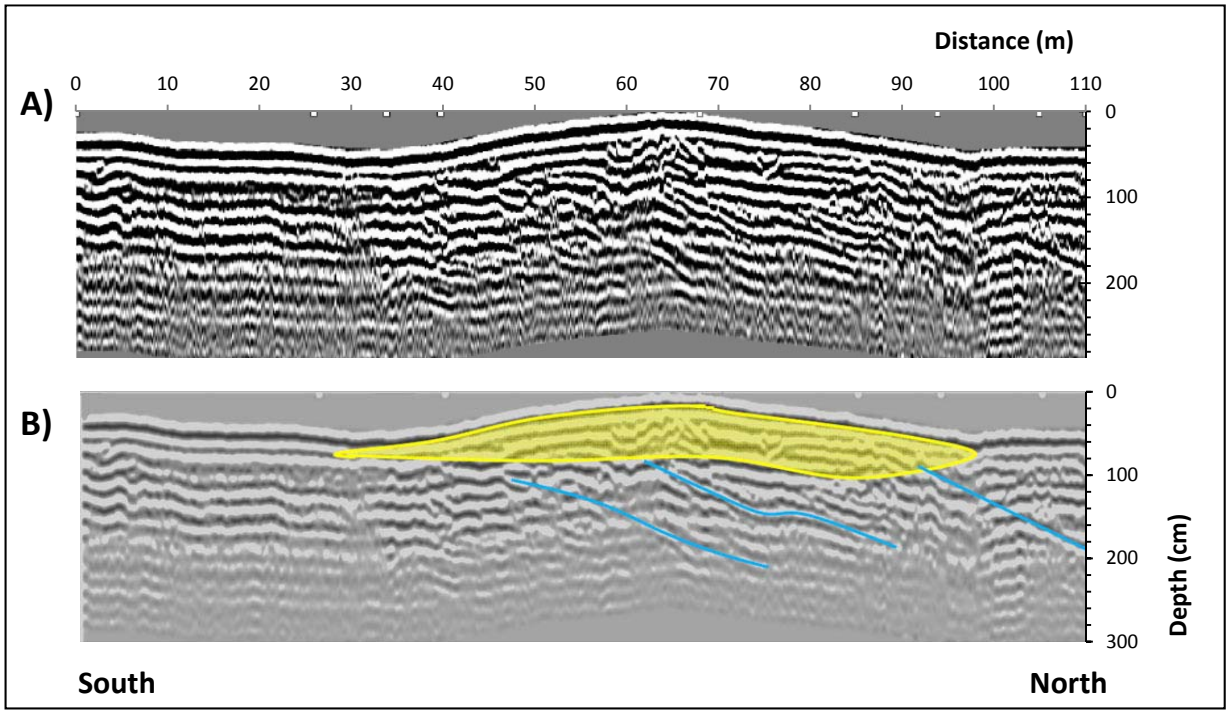

Figure 8: **A**: GPR profile and **B** the relatively horizontally deposited structure (yellow), which can be interpreted as aeolian dune deposits, with a few clear dipping reflector layers (blue).

T.G. Winkels
Faculty of Geosciences
Utrecht University
Department Physical Geography

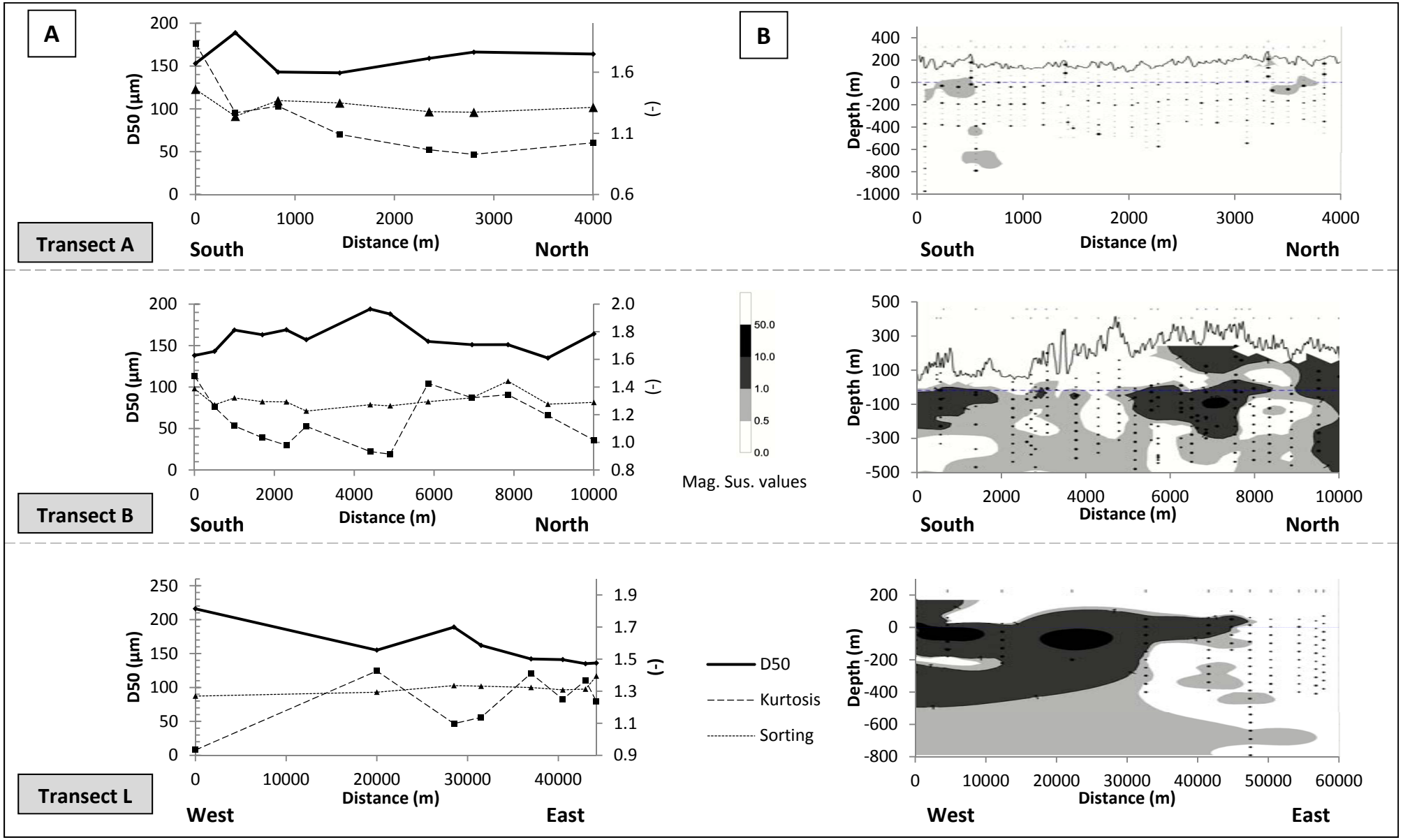

Figure 9: **A:** different grain-size parameters (D50, sorting, kurtosis) values along the three different transects. **B:** Magnetic susceptibility values measured at different depths, along the three different transects

Magnetic susceptibility values stay rather low throughout the entire section, although some samples show slightly elevated values around the groundwater table.

Transect B Grain-sizes (D_{50} values) show a gradual increase, from the most southern cores towards the north. Simultaneously, kurtosis values decrease significantly and sorting values increase slightly. In more northward direction the sorting coefficient keeps increasing slightly while kurtosis values first show a significant increase before gradually decreasing again. Grain sizes gradually decrease in more northward direction before increasing significantly in the most northern core. Magnetic susceptibility values show large scale variability throughout the entire transect. However, samples taken around the groundwater table show elevated values throughout the entire section. The most southern and northern cores show the highest magnetic susceptibility values.

Transect L D_{50} values decrease significantly in southward direction, while sorting coefficients stay rather constant along the entire transect. Although kurtosis values fluctuate flowing a show saw-tooth pattern, a general increasing trend can be distinguish. When looking at magnetic susceptibility values, these decrease significantly in eastward direction with highest values located around the groundwater table.

5.3 Sedimentary Zone classification

Beach ridges develop in propagation coastal regions from sediments transported their by the different rivers systems and/or by coastal processes. However, when looking at the Usumacinta-Grijalva delta, the micro tidal regime in combination with relatively small waves lead to the assumption that present day coastal processes are irrelevant for when looking at sediment origin. River systems are thus regarded as the dominant source of sediments used for beach ridge formation. Rivers channels are however not fixed in the delta plain. River meandering cause's small scale changes in river position, while avulsions can lead to large scale relocation of river channels.
With LIDAR images (INEGI, 2008) the orientation and cutoffs of different beach ridges are determined to define periods (i.e. zones) during which the position and discharge (distribution) of the multiple river channels was relatively stable. For the resulting zones the following sedimentary characteristics, *D_{50}/sorting/kurtosis/magnetic susceptibility*, are compared to see whether these different sedimentary proxies support this subdivision and can possibly be used to further enhance this subdivision. Due to longitudinal variations, the zones were compared between the different transects (Transect West and East). A detailed summary of the different grain-size parameters and magnetic susceptibility values for each zone can be found Appendix 7.

Zone 1 Zone 1 is located in the south-western part of the delta (Fig. 10). All values related to grain-size were computed during the field campaign of 2012. Due to the use of different analytical methods in 2012 and 2013, comparison between these two different

T.G. Winkels
Faculty of Geosciences
Utrecht University
Department Physical Geography

datasets is difficult. However, magnetic susceptibility (measured in 2013) values show overall low values (Appendix 7).

Zone 2 Zone 2 is located in the southern part of the delta (Fig. 10) west of the current main river branch. Upper grain-size distributions show well sorted deposits with low magnetic susceptibility values. Grain-size distributions for cores (192 & 453) located at the zone boundary show a deviating grain-size signal. Magnetic susceptibility for these cores is significantly higher when compared to other cores, especially for the upper samples (Appendix 7). Deviating core is core 449, which is situated in the middle of the zone and is characterized by extremely high magnetic susceptibility values in 300cm below surface level sample (Appendix 7).

Zone 3 Zone 3 is located in the mid-eastern part of the delta (Fig. 10). Compared to zone 2, deposits in zone 3 are relatively fine and well sorted sediments. An exception is core 188, which shows a bimodal grain-size distribution (computed following the 2012 grain size method). However, magnetic susceptibility values are generally higher in zone 3, with maximum values in the upper samples of core 188 (Appendix 7).

Zone 4 Zone 4 is located in the middle-part of the delta (Fig. 10), stretching over almost the entire width of the present day delta (West – East) although no cores were taken East of the present river channel during the 2013 field campaign. Beach ridges east of the main river channel are however less clear when looking at the LIDAR images. Zone 4 shows a clear shift towards coarser grain-size distributions compared to zone 3. Examination of the upper samples show clear unimodel distributions while lower situated (300cm below surface level) samples show a gradual increase in coarser grain-size class (around 231µm), eventually leading to bimodal distributions. Lowest samples (500cm below surface level) show an additional increase in an even coarser grain-size class (400µm) (Appendix 7). Zone 4 is characterized by highly fluctuating magnetic susceptibility values.

Zone 5 Zone 5 is located in the northern part of the delta (Fig. 10), stretching over almost the entire width of the present day delta (West – East). During the field campaign of 2013 cores were taken on both the West and East side of the river channel. Zone 5 is characterized by slightly better sorted grain-size distributions, compared to zone 4. Magnetic susceptibility values show far less variability compared to zone 4, with exception of core 447, which shows higher magnetic susceptibility values for the upper samples. Examining the regional patterns, major differences in grain-size distributions and magnetic susceptibility values throughout the entire zone become apparent. Cores taken along the eastern transect show a complex grain-size distributions pattern. These samples are characterized by bimodal distributions, with their main peak at 165µm and a secondary peak around 231µm. Grain-size distributions show a gradual increase in this coarser secondary class in cores taken in northward direction. Simultaneously, sorting coefficients also increase gradually in northward direction.

When looking at magnetic susceptibility values, values seem to decrease significantly in

T.G. Winkels
Faculty of Geosciences
Utrecht University
Department Physical Geography

eastward direction with highest values are measured in cores 461 and 462 and lowest values in cores along the eastern transect cores (Appendix 7).

Zone 6 Zone 6 is located in the north western part of the delta (Fig. 10), and corresponds with the most recent period of delta build-up. During the field campaign of 2013 cores were taken of both the east and west side of the present river channel. Cores in Zone 6 are characterized by a generally finer sediment signal compared to zone 5. However when comparing grain-size distributions between cores taken west or east from the river, cores taken west of the river are slightly coarser (west modus = 137.5µm and east modus = 165µm). Core 428 shows a totally different signal, with clear bimodal distributions at 150cm below surface level (D_{50} = 219µm) and a significantly finer signal (D_{50} = 113µm) for the 300cm below surface level sample.
Magnetic susceptibility values are slightly elevated throughout all cores and depths compared to zone 5. Core 443 is characterized by two significantly higher peaks values around 150cm and 500 cm below surface level, while cores 429 and 430 show only peaks values in samples taken 150cm below surface level (Appendix 7).

Zone X Zone X is located the north eastern part of the delta (Fig. 10). No cores where taken from within this zone, during the field campaigns of 2012 and 2013. Therefore, no information about the sediment characteristics is available for this zone. The distinction of this zone is solely based on LIDAR images.

T.G. Winkels
Faculty of Geosciences
Utrecht University
Department Physical Geography

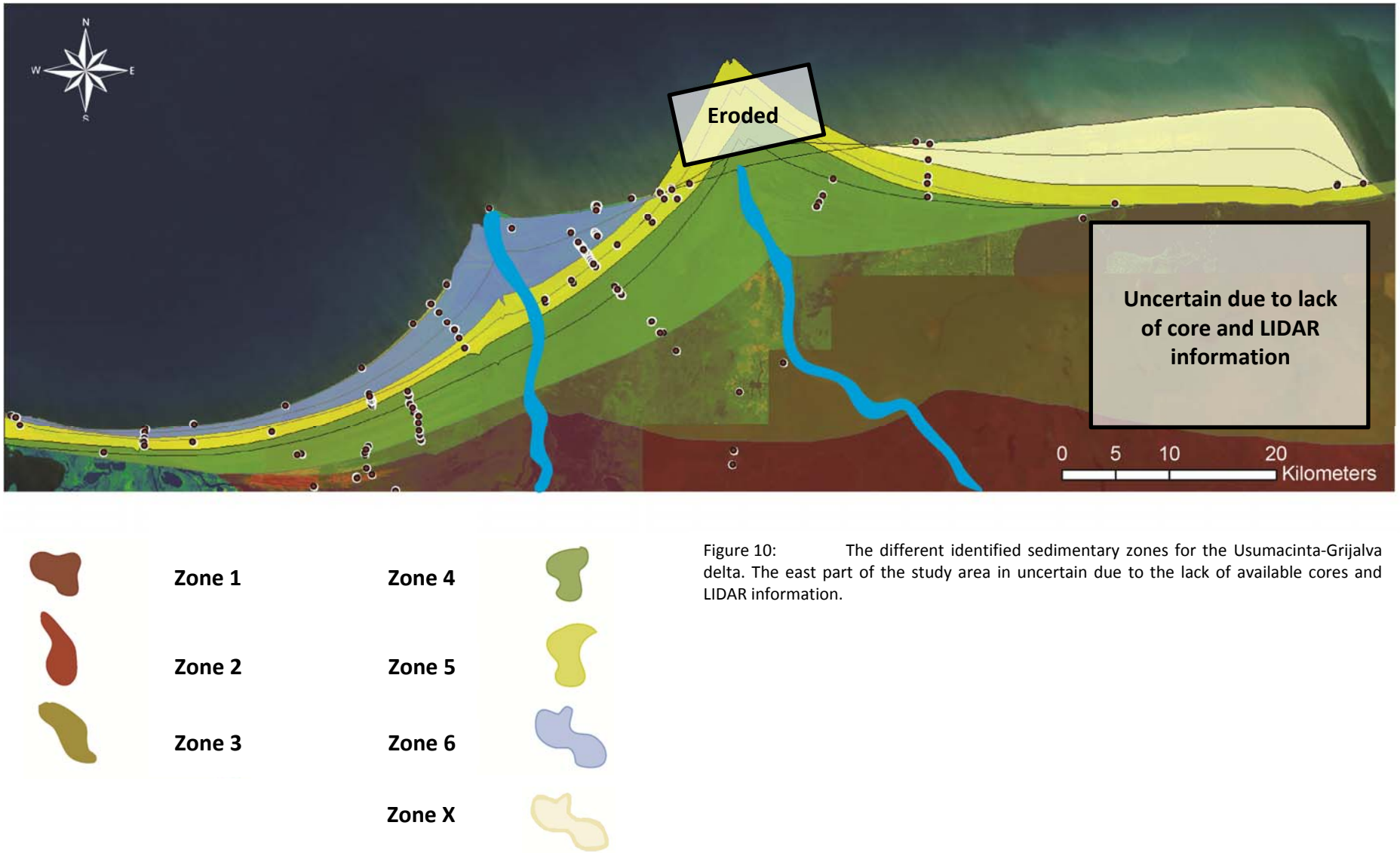

Figure 10: The different identified sedimentary zones for the Usumacinta-Grijalva delta. The east part of the study area in uncertain due to the lack of available cores and LIDAR information.

T.G. Winkels
Faculty of Geosciences
Utrecht University
Department Physical Geography

5.4 End Member Modeling

5.4.1 Choosing number of end-members

Coefficients of determination (r^2) form the basis for determining the goodness of fit for a specific End Member (EM) model. Coefficients of determination were calculated for the individual grain size classes for both datasets (Fig. 11A).

For the *sieve* dataset the majority of the sediment concentrates between the range 75µm and 300µm. Reproducibility of these grain-size classes is most important. When looking at the two EM model (EM2), which shows low r^2 values around 150µm (Fig. 11A1), it fails to meet the required reproducibility in dominant grain-size range. A three EM model (EM3) already shows a significant increase in r^2 values for the dominant grain-size range, increasing from 0.52 to 0.78 (Fig. 11B1). When comparing the EM3 model to the EM4 model the latter still shows a significant increase in r^2, increasing from 0.78 to 0.84, for the dominant grain-size range. Coefficients of determination values keep increasing when looking at a five EM model. However, a six end member model (EM6) fails to increase the goodness of fit when compared to the five end member model (EM5) (Fig. 11A2). Hence a four or five EM model (EM4-EM5) can best be used explain the variation in the *sieve* dataset.

For the *laser* particle analyzer dataset the majority of de sediment concentrates between 75µm and 354µm. When looking at the two and three EM model (EM2 & EM3) they show low r^2 values around 177 and 210µm, thus failing to meet the required reproducibility in main grain-size classes (Fig. 11B1). When comparing the r^2 values for the four, five and six EM models (EM4- EM6), they produce better but similar results. Running a higher order end member model does not result in a better explanation of the mixed dataset (Fig. 11B2). Hence a four end member model (EM4) can best be used to explain the variation in de laser particle analyzer dataset. In order to compare results of the two different datasets a similar EM model has to be used for both datasets. Thus, based on the coefficients of determination, a four EM model (EM4) was chosen to unmixed the two datasets.

5.4.2 End-member characteristics

Each specific end-member can, based on their distribution characteristics, be linked to specific processes. Comparison between different end-members was done using various grain-size parameters (Appendix 8).

Sieve End-Members

The resulting four end-members, except for EM3, are all characterized by *bimodal* distributions. However, there is a significant difference in the type of bimodal distribution. For EM2 both peak values represent comparable abundances, respectively 30% and 27% of the total volume. End-members 1 and 4 show significant differences between abundances of these peak values (Fig. 11C).

T.G. Winkels
Faculty of Geosciences
Utrecht University
Department Physical Geography

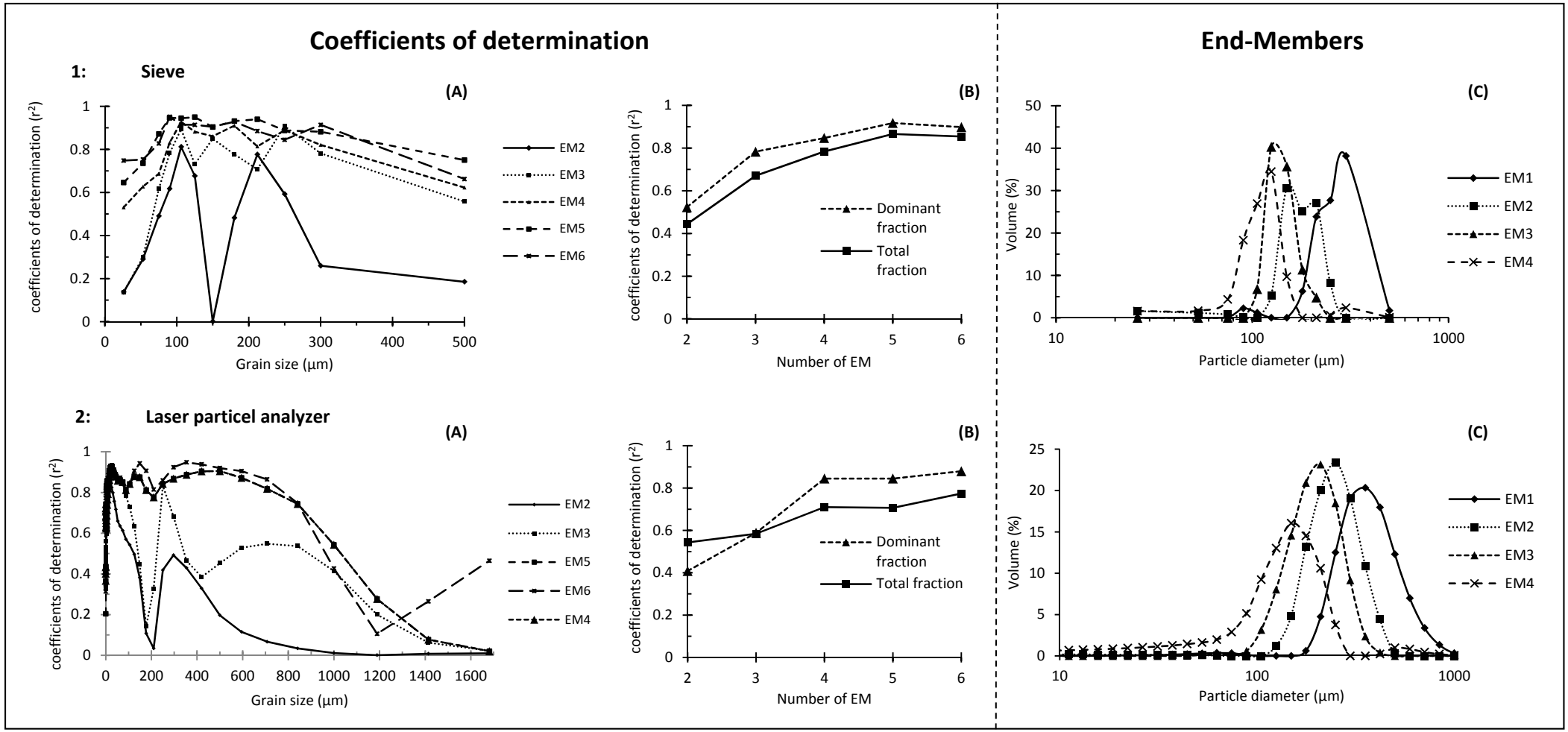

Figure 11: **A:** the coefficients of determination (r^2) for the different end-member models over the measured grain-sizes for both the sieve (1) as the laser particle analyzer (2) dataset. **B:** the mean coefficients of determination (r^2) for the different end-member models for both the entire grain size range as the dominant (Sieve: 75-300µm; Laser 75-354µm) sediment fraction both the sieve as the laser particle analyzer dataset.

T.G. Winkels
Faculty of Geosciences
Utrecht University
Department Physical Geography

Laser End members

Opposite to the sieve end members, the resulting four end members for the laser dataset, except for EM4, are all characterized by *unimodel* distributions. EM4 is characterized by a bimodal distribution, with one dominant peak value at 150µm.

Comparison between the end members of the two datasets shows that end members computed from the laser dataset set are significantly coarser than the end members computed for the sieve dataset. Besides this offset in coarseness, laser end members show a more spread-out distribution (Fig. 11C) while the abundances of the individual end members show a tendency towards coarser end members (Fig. 11C).

5.4.3 End-member abundances

As each individual end-member reflects a different sediment population, changes in abundances of these end-members reflect changes of the ratio between these sediment populations. By plotting end-member abundances along the three different transect, this ratio between the different sediment populations is analyzed.

Transect A Transect A can be subdivided into three different sections; section 1 = core 429 – 378, section 2 core 387 – 393, section 3 core 429. Due to the higher resolution of the analysis, laser data EM abundances show a significantly higher variability (Fig. 12). Despite these differences after processing both datasets, similar trends occur in EM abundances. Section 1 is characterized by a gradual increase in EM4. EM2 values stay rather constant throughout this section. Section 2 shows a significant increase in EM2 values an decrease in EM4 abundances. Again EM2 values and EM1 values stay rather constant. Section 3 shows an increase in again the finer end members EM3 and EM4. Besides these similar trends there are some significant differences between the two datasets. For section 1; Laser abundances show a significant increase in the contribution of EM1 for cores (395, 396 and 397) while EM2 values vary greatly throughout this section, while sieve abundances show an, almost negligible, constant signal in EM1 and EM2 (Fig. 12).

Transect B Transect B can be subdivided into three different sections; section 1 = core 432 – 433, section 2 = core 434 – 440, section 3 core 447 – 444. Due to the higher analyzing resolution, sieve data EM abundances show a significantly higher variability for north section of the transect (Fig. 12). However, both transects do show similar trends in the end member abundances. The first section is characterized by high EM3 and EM4 abundances. The second section shows a rapid increase in EM2 abundances. Exception is core 436, where both datasets show a decrease in EM2 abundances. While the third section is characterized by a decrease of these same coarser end members. Besides these similar trends there are some significant differences between the two datasets. For the first section; EM1 values in sieve abundances stay negligibly low, with exception of cores 439 and 440 where EM1 values show a small increase. The increase of coarser end members is thus solely reflected by changes in EM2 abundances,

T.G. Winkels
Faculty of Geosciences
Utrecht University
Department Physical Geography

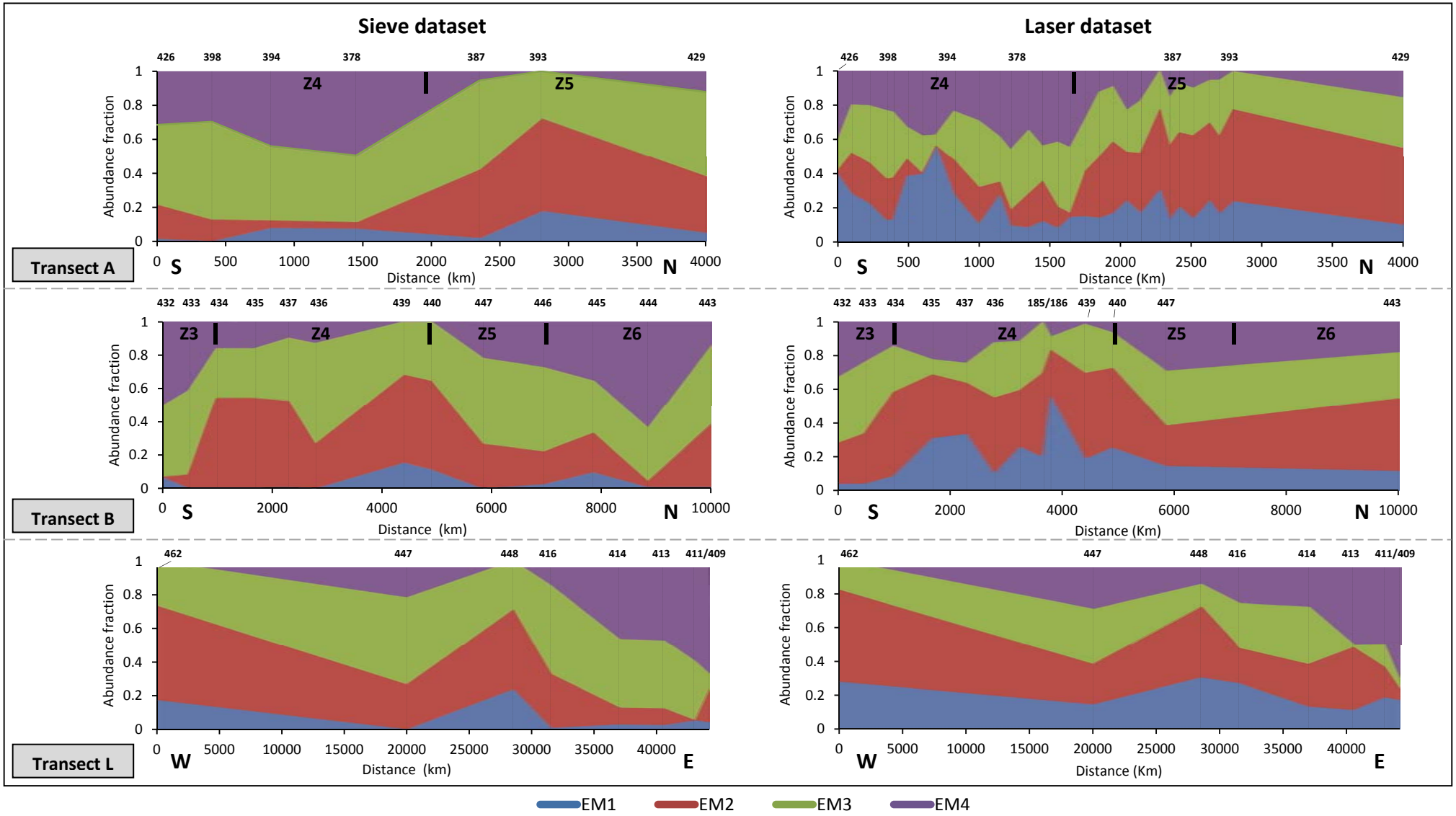

Figure 12: Different end-member abundances (EM1 = Blue, EM2 = Red, EM3 = Green and EM4 = Purple) across three different transects; Transect A, Transect B and Transect L, for both the sieve as laser dataset.

T.G. Winkels
Faculty of Geosciences
Utrecht University
Department Physical Geography

at while for the laser abundances EM2 stay rather constant and most variation can be explained by changes in EM1 abundances. Core 186, absent in sieve transect, shows a sudden increase in EM1 values (Fig. 12). Comparisons between the different datasets for the most northern part of the transect impossible due to lack of laser analyzed cores.

Transect L Instead of perpendicular towards the beach ridges, transect L runs parallel to a single beach ridge, reflecting the changes in EM abundance along a (paleo) coastline. Transect L can be divide into three different sections; section 1 = core 462 – 447, section 2 core 448, section 3 core 416 – 409. In contrast to the other transects, similar cores where analyzed for both datasets (Fig. 12). The first section is characterized by a decrease in the coarser end members (EM1 and EM2. The second section shows a rapid increase in the abundances of EM1 and EM2 (core: 449). The third section is again characterized by a significant increase in the abundances of the finer end members. Besides the higher abundances of EM1 in the laser transect, only core 409 shows a deviating signal. Sieve abundances show a sudden increase in EM2 which is not present in the laser abundances (Fig. 12).

5.5 Depth variations end members

When comparing EM abundances it is important to have an insight of the internal variations in EM abundances throughout a signal core. Large scale variations within a signal core could make it impossible to identify trends. In order to exclude that observed trends are the result of internal sediments variations, EM abundances have been plotted for different depths (150cm and 500cm below surface level) along the multiple transects and compared to the original transect (300cm-mv). In addition, the EM abundances are plotted for a two individual cores.

Figure 13A shows the EM abundances for core 426 and the combined 399 and 427 core (correlation was done using the water table as a reference height). Striking is that EM abundances in the combined cores of 399 and 427 are relative constant. Only at 630 cm below surface level, EM1 abundances show an increase. Core 426, however, shows a notable amount of internal variation in the EM abundances. EM1 increase significantly at both 300cm and 900cm below surface level. EM4 values also show a significant amount of variation. These internal variations are the result of sorting/buildup processes that determine the internal sedimentary characteristics of an individual beach ridge. Despite these internal variations, a transect plotted for different depths does show similar trends. Figure 13B shows the EM abundances, for different depths, along transect B. All transects show an initial increase in the coarse end members (EM 1 and/or EM2) followed by a significant decrease of these same end members. In the second section, these same end members show an increase. Despite these similarities, there are some significant differences in the rate at which these changes occur on different depths. At 150cm transect, EM2/EM4 values increase/decrease rapidly between cores 437 and 436 while at 300cm below surface level, EM1 and EM2 values increase, and EM4 values decrease gradually to their maximum/minimum values between cores 437 and 440(Fig. 13B). Afterwards al transects show an increasing trend in the finer end members. All these trends are comparable to the trends found in the original transect A (5.2.3 Sieve data) and this also applies to the other

T.G. Winkels
Faculty of Geosciences
Utrecht University
Department Physical Geography

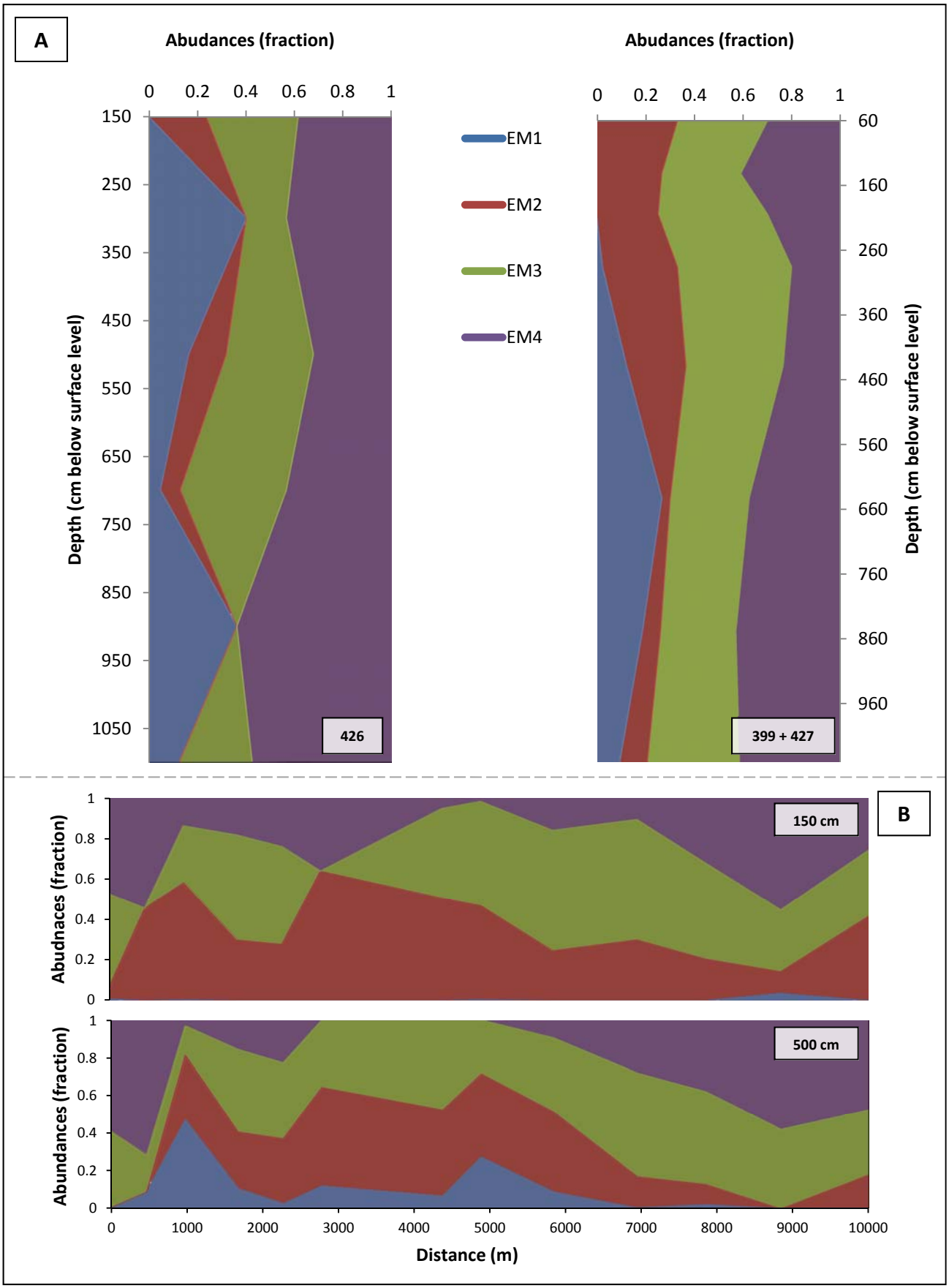

Figure 13: **A:** EM abundances throughout two cores (426 and combined core 399/427). **B:** EM abundances along transect B for both samples taken from 150cm and 500cm below surface level.

T.G. Winkels
Faculty of Geosciences
Utrecht University
Department Physical Geography

transect as well. Conclusion is that although the precise internal structure of an individual beach ridge is not known and some internal variation is present, trends shown in EM abundances for the multiple transect depths are similar.

5.6 Heavy minerals

Heavy minerals were examined in order to determine sediments provenance. A small selection of samples was investigated (Fig. 14) resulting in that any conclusions drawn in this section should be handled with care. In this section the applicability of heavy minerals in determining sediment provenances for the Usumacinta-Grijalva delta is examined.

5.6.1 Heavy mineral percentages

Grijalva reference samples

Samples taken upstream in the Grijalva (Fig. 14). are characterized by a high percentage of heavy minerals. A high percentage of these heavy minerals (over 40%) are characterized magnetic minerals (Fig. 14).

Usumacinta reference samples

Due to the lack of analyzed upstream Usumacinta samples core 470 (Fig. 14), taken from a beach ridge located in the most east side of investigated area, was assumed to represent Usumacinta sediment. Examination of core 470, showed a very low heavy mineral percentage (<2%) and an absence of magnetic minerals (i.e. magnetite) (Fig. 14), which is expected based on the source area.

Transect L

Along transect L heavy mineral percentages decrease gradually is eastward direction. Heavy minerals percentage in the western core can be as high as 10% while eastern cores only show percentage of around 3 to 5%. The magnetic mineral percentages show a similar pattern, with higher values in the west compared to the east. Exception to this trend can be found in core 448 and 416. Magnetic mineral percentages drop to 0% in core 448 and increase again to around 5% in core 416. The most eastward core (409) also shows a deviating signal, with significantly increasing magnetic mineral percentages (Fig. 14).

5.6.2 Heavy mineral determination

Grijalva reference samples

In total two Grijalva reference samples were counted. These samples are characterized by low percentages of opaque minerals (Fig. 15). Identification of the remaining non opaque grains revealed that percentages of green and brown *amphibole* minerals are relatively high in these reference samples, with a tendency to higher percentages of brown *amphiboles* in relation to the green *amphiboles*. *Titanite* and *hypersthene* seem to be present in equivalent quantities while volcanic *augite* percentages show a significant spike in only the Grijalva_bed sample (Appendix 9).

T.G. Winkels
Faculty of Geosciences
Utrecht University
Department Physical Geography

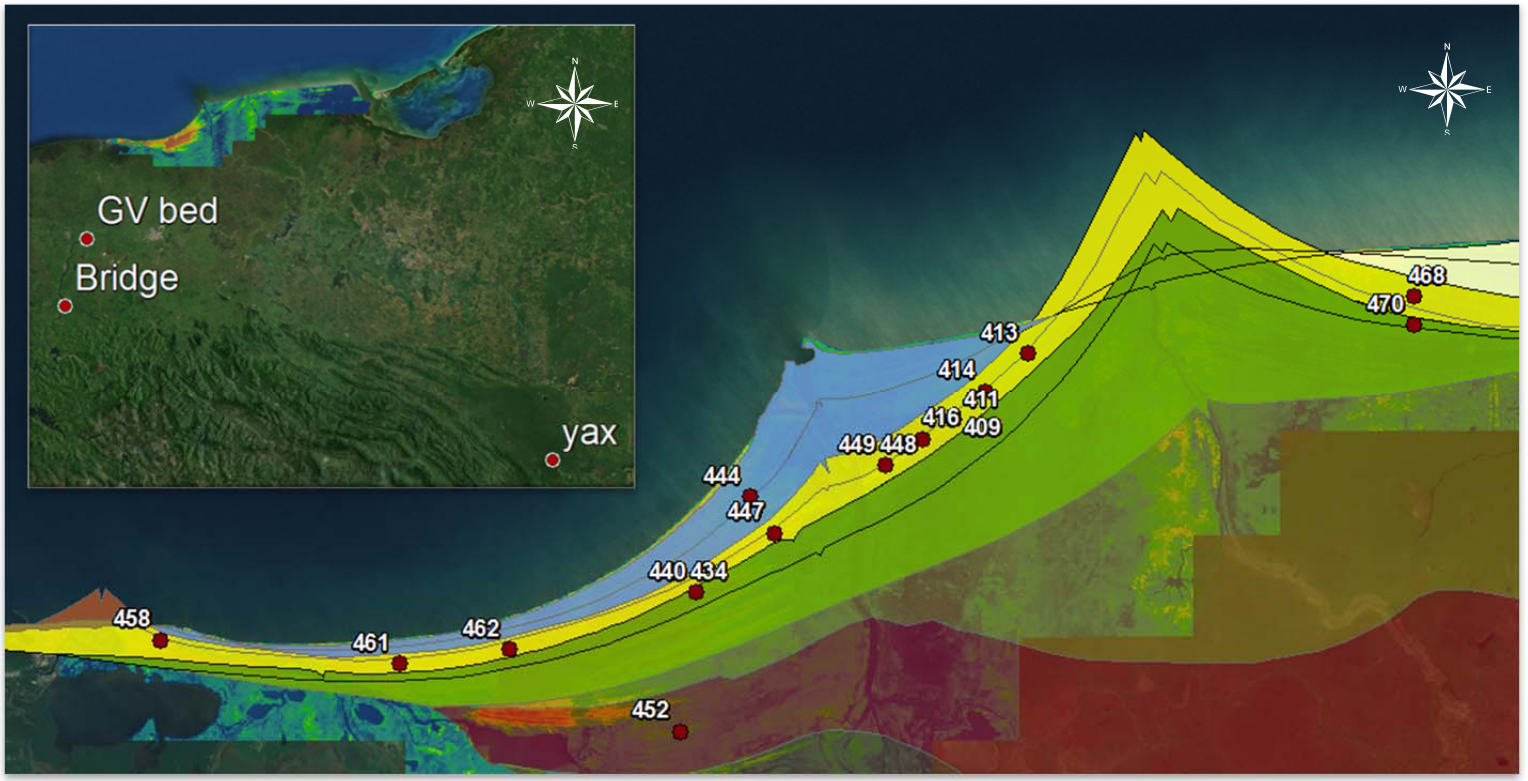

Samples	HM (%)	Magnetic (%)	Samples	HM (%)	Magnetic (%)
409	2.51	9.38	449	77.25	30.91
411	4.47	1.56	452	82.93	0.00
413	4.31	2.44	458	22.22	27.27
414	5.58	5.71	461	5.77	33.33
416	4.74	5.56	462	8.11	16.67
434	35.92	5.41	468	3.57	10.53
440	2.00	0.00	470	1.36	0.00
444	48.30	1.22	Bridge	10.12	40.00
447	7.14	5.88	GV bed	10.29	57.14
448	6.74	0.00	yax	15.21	12.23

Figure 14: **A**: Percentage heavy minerals and the percentage of magnetic minerals present in the samples. **B**: Location of heavy minerals samples taken throughout the delta.

Usumacinta reference samples

Only one Usumacinta reference sample was counted. This sample is characterized by high percentage of opaque minerals, approximately 70% (Fig. 15). Identification of the remaining non-opaque grains showed a relative low percentage of green and brown *amphibole* minerals and a high percentage of *epidote*. The percentage of *granate* and *spinel* minerals is also significant. *Zircons* are also present, although not in large quantities (Appendix 9).

Delta samples

In total two delta samples were counted from different sides of the delta. Sample 462 shows a high percentage of green and brown *amphibole* minerals and a significant contribution of *augite*, *titanite* and *epidote minerals*. Core 409 shows a large percentage of green *amphibole* minerals and is also characterized by the presence of a substantial amount on *spinel (*Appendix 9).

5.4.3 Heavy mineral comparison

Comparison between different cores reveals some significant differences. When comparing the ratio between green and brown *amphibole* it seems that, reference Grijalva samples and possibly Grijalva delta sediments samples have the tendency incorporate more brown than green *amphiboles.* While samples linked to Usumacinta, sediments have the tendency incorporate more green than brown *amphiboles.* The presence of *spinel* can also possibly be used as a trace mineral, as these were only found in sediments linked to Usumacinta system (Yax and 409). Magnetite can also possibly be used as a trace mineral. The highest magnetite percentages were found in a sample (3m Terras) upstream of the Grijalva near the *El Chichón* volcano. Here almost 90% of the heavy minerals were magnetite minerals. The lowest magnetite percentages were found in the Usumacinta reference sample (Yax); hence it looks like magnetite finds it origin from the volcanic sediments transported by the Grijalva.

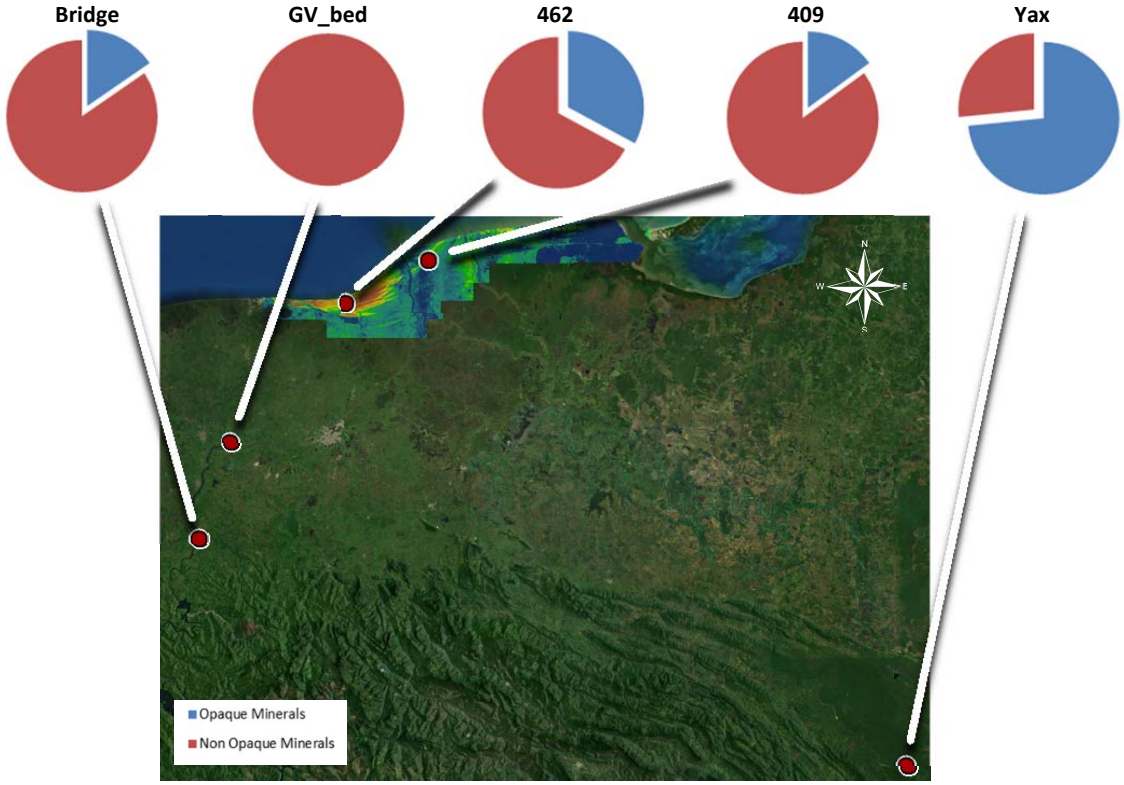

Figure 15: Ratio between of opaque and non-opaque minerals for 5 different samples.

5.7 End-member labels

Based on provenance and sorting processes, a physical meaning is assigned to each specific sediment population (end-member). End-member distributions were compared to reference samples of which, based on their location, the provenance is known (e.g. upstream samples). Based on this comparison the coarser end-members (EM1 and EM2) seem to be related to the Grijalva river system, while the finer end-members (EM3 and EM4) are related to the Usumacinta river system.

EM1 & EM2 Related to Grijalva sediments

EM3 & EM4 Related to Usumacinta sediments

It is possible that the allocation of these labels is affected due to changes in river provenance and/or extensive (secondary) sorting processes. Changes in river provenance are assumed to have a negligible effect on the sediment populations of both river systems as geological settings in the different drainage basins is rather universal. Hydrodynamical changes (i.e. river length) of the individual rivers can have an impact on rivers sediment populations.
Bye extensive (secondary) sorting, sediments are exposed to coastal processes for a longer than an average period, and can have a strong effect on the sediment populations. It is thus important to keep these factors in mind, when interpreting EM abundances.

5.8 Sorting processes

Although coastal processes do not play an important role in sediment delivery they do however play an important role in sediment reworking, eventually determining the sedimentary characteristics of beach ridge sediments. These processes selectively transport sediments perpendicular and along to the (paleo) coastline. Two coastal sorting processes discussed here are *longshore* and *perpendicular* coastal sorting processes.

Longshore sorting processes

Longshore transport plays an important role in distributing sediments, necessary for beach ridge formation, along the coastline. Evidence for the dominant direction of longshore currents can be found in the presence of beach ridges in the eastern part of the study area, Zone X (Fig. 10). There is no river to act as a primary sediment supply in this region; hence the source of these sediments has to be the eroded former Usumacinta delta lobe. Due to the dimensions and strong progradation in this zone and absence of similar features in the western part of the delta it is assumed that dominant longshore currents are towards the east.
When looking at the origin of these longshore currents it is important to look at the dominant wind direction in combination with coastline orientation. These influence the angle/orientation in which waves hit the coast, inducing longshore currents. However, prevailing east winds in the Gulf of Mexico make it difficult for a dominant eastward longshore current to develop. Easter longshore currents can possibly be linked to the *Nortes* (see section: *3.1 Climate setting*).

T.G. Winkels
Faculty of Geosciences
Utrecht University
Department Physical Geography

Although these *Nortes* only occur a few times each year, it is possible that due to their severity they have a dominant impact on sediment transport. This was however not thoroughly investigated, so the precise origin of the direction of these longshore currents remains unclear.

Perpendicular sorting processes

Examination of the coastal profile showed a clear sorting pattern perpendicular to the coast (Fig. 16). The underwater section of the coastal-transect (-50m:-230m) is characterized by significantly lower D_{50} values compared to the beach section (100m:-50m). This pattern is characteristic for a shoreface-beach profile, as waves transport the sediment up de beachface were it is sorted by swash and backwash currents (Hoekstra, 1997). It is possible that these perpendicular processes can explain variability in EM abundance throughout a signal beach ridge (*5.5 Depth variations end-members*).

Erosion phases

During aggradation conditions, *longshore* and *perpendicular* coastal sorting processes are assumed to be rather constant. It is possible that due to changes in coastline orientation longshore currents are affected, however examination of cores did not indicate any evidence for this. When the coastline changes from an aggrading to an eroding system, selective transport of sediments erosion by coastal processes leads to significant change in both, beach ridge morphology as sedimentary characteristics of the remaining beach ridge. This can for example lead to the concentration of magnetite. Relatively high magnetic susceptibility values, indicating high magnetite abundances, in combination with beach ridge morphology were thus used as indicator for phases of past coastal erosion.

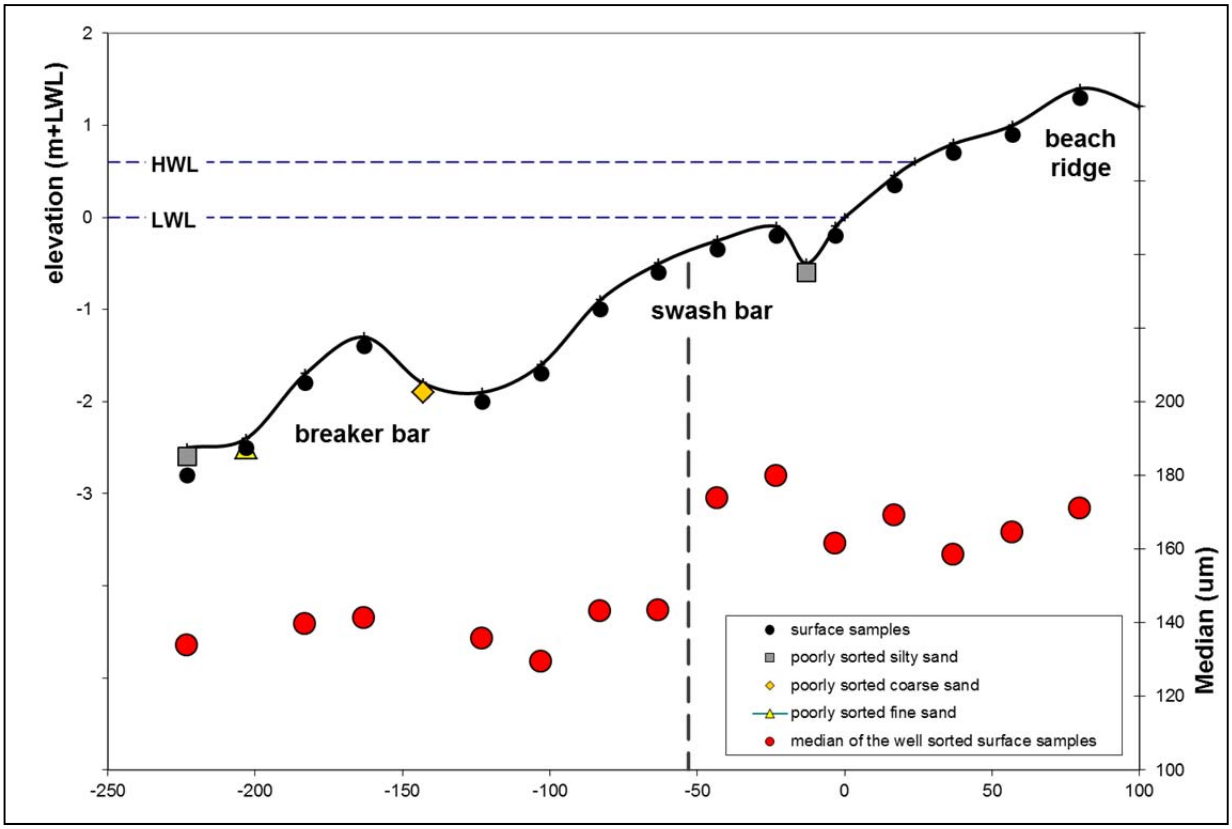

Figure 16: Coastal profile indicating the different surface samples (black) and the different median grain sizes (red).

T.G. Winkels
Faculty of Geosciences
Utrecht University
Department Physical Geography

5.7 Age models

Multiple age models were constructed along the two different transects; transect A and transect B. For the construction of the different age model only ^{14}C dates were used. Age models were constructed by fitting multiple high order polynomial functions, for multiple sections, through calibrated ^{14}C ages (Fig. 17). OSL samples taken during the field campaign of 2013 are still in preparation and are thus not incorporated into these age models.

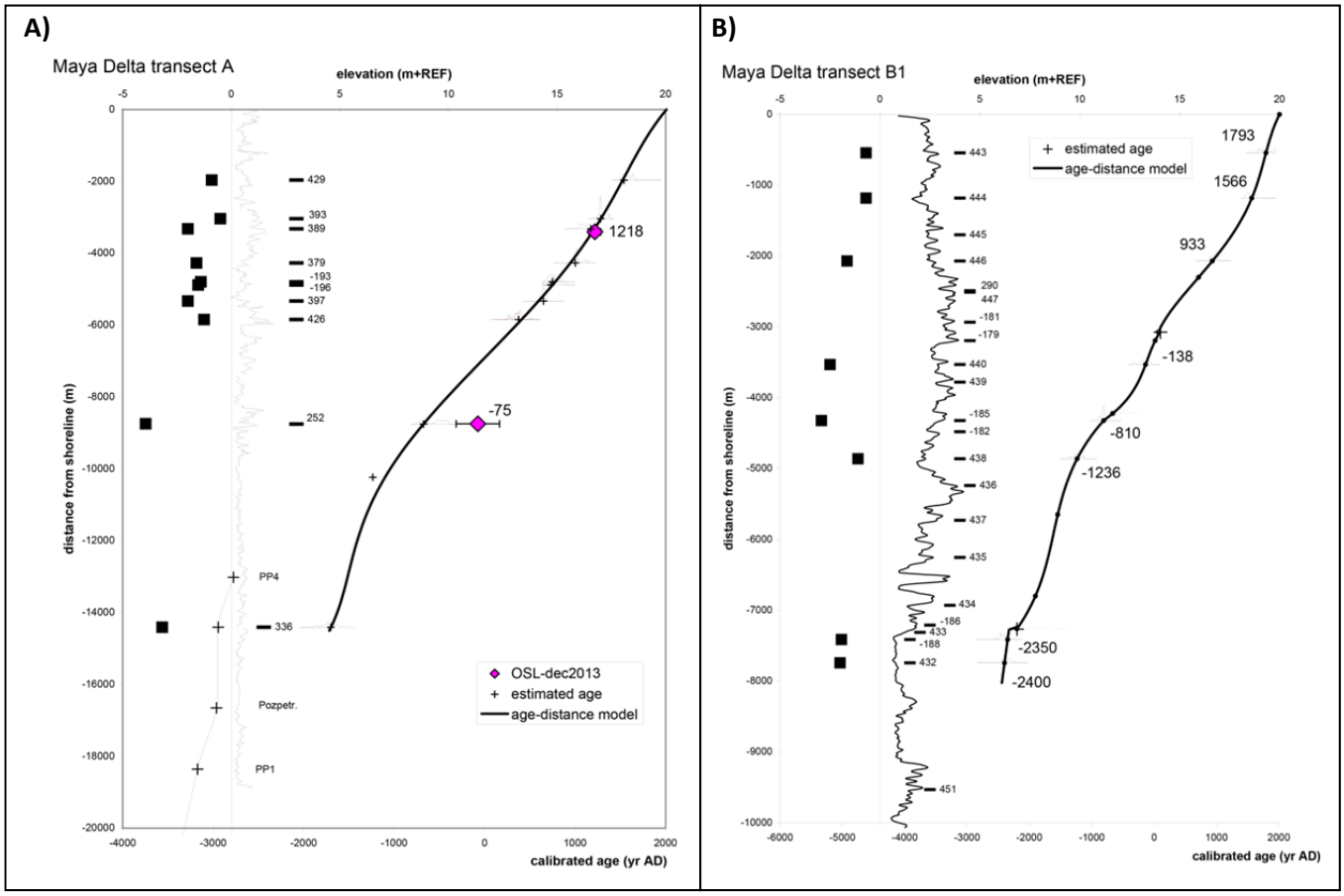

Figure 17: Age models constructed along transect A (A) and transect B (B) using calibrated 14C ages.

T.G. Winkels
Faculty of Geosciences
Utrecht University
Department Physical Geography

6. Paleogeographic evolution of the Usumacinta-Grijalva delta

The Usumacinta-Grijalva delta is characterized by the largest beach ridge plain in the world. These beach ridges are formed by coastal processes with sediment delivered there by the two main river systems; Usumacinta and Grijalva. Using the analyzed beach ridge deposits five different phases of delta evolution could be identified, which are presented below (see also Fig. 17).

Phase 1 *Age: >3000 BC – 2500 BC*

Phase 1 covers the initial period of beach ridge formation and can be correlated with sedimentary zones 1 and 2. Throughout the evolution of the delta, the Grijalva River can be regarded as a river with multiple channels while the Usumacinta has only one dominant channel throughout almost the entire evolution of the delta. Located just west of the study area is the *Rio Seco* which, based on historical maps, was an important branch of the Grijalva until at least late 16th century. The main channel is located in the south central part of the study area (Fig. 18). The oldest investigated beach ridges are formed along this channel. These ridges are composed of relatively coarse sediment, corresponding with the sediment properties of the Grijalva (core 453). In a later stadium this secondary channel bifurcates resulting in development of beach ridges at two different locations (Fig. 18). End member modeling on single cores showed a dominant contribution of coarse end-members, supporting the assumption that the Grijalva was still responsible for the delivery of sediments forming these beach ridges.

Core 192, located at the boundary of phase 1, indicate high magnetic susceptibility values which can possible be explained by a period of erosion and/or volcanic activity. Determining which of these two processes is responsible for the increased values is impossible due to the limited amount of cores taken in this section.

Previous research (2012) showed that the eastern part of the delta represents a large *chenier plain*. However, due to the lack of available data, it is impossible to pin point the exact time of origin of these first beach ridges and *cheniers*.

Phase 2 *Age: 2500 BC – 1700 BC*

Phase 2 covers the period ranging from 2500 BC to 1700 BC and can be directly correlated with sedimentary zone 3. Beach ridges formed during this phase show a significant change in sedimentary characteristics. Analyzed cores show that the coarser signal of the Grijalva has almost entirely been replaced by the (finer) sediment signal which can be related to the Usumacinta system. Apparently discharges of the secondary Grijalva channels decrease significantly during this period, resulting in a drop in sediment supply and the abandonment of the secondary channel of the Grijalva. Beach ridges formed during this phase are composed out of sediment related to the Usumacinta system which is transported along the coast by alongshore currents. Dating of cores 432 and 336 put this phase of delta evolution between 2500 – 1700 BC.

T.G. Winkels
Faculty of Geosciences
Utrecht University
Department Physical Geography

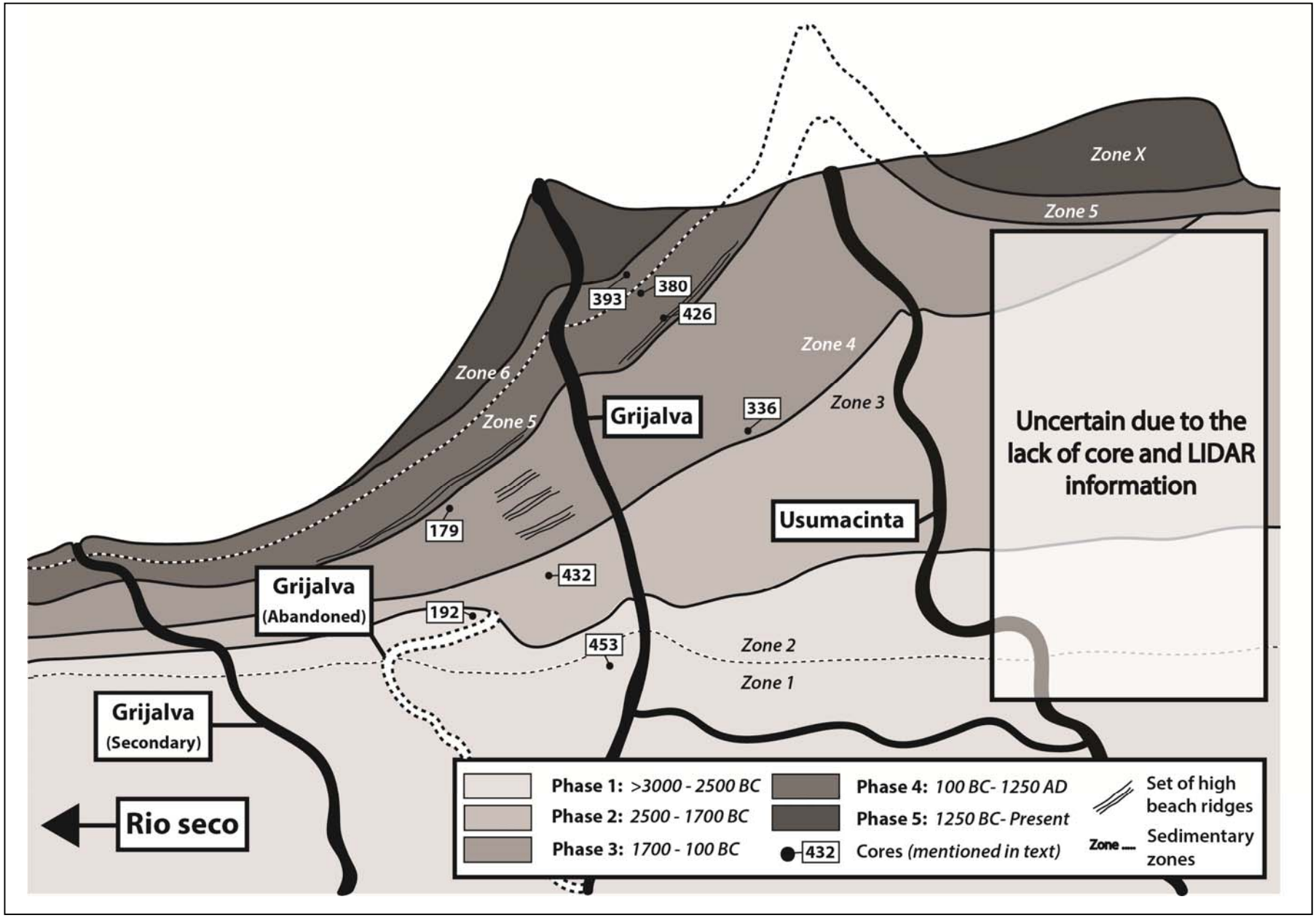

Figure 18: Different phases of progradation for the Usumacinta-Grijalva delta with correlating sedimentary zones.

Phase 3 *Age: 1700BC – 100BC*

Around 1700 BC the first recognisable beach ridges are formed in the eastern part of the delta. End member modeling one these beach ridges, shows a clear Usumacinta signal. However, a small percentage of coarse end members indicate there is a limited contribution of Grijalva sediments transported there by longshore currents. During the same period, in the western part of the study area, the old secondary Grijalva channel becomes more dominant again whilst a new secondary channel starts transporting sediments towards the north east (Fig. 18).
As delta progradation continues, LIDAR images clearly show that beach ridges developed in the eastern part of the delta are significantly lower compared to beach ridges formed in the west (Fig. 5). In the west a clear pattern between sequences of high and low beach ridges becomes visible. In order to determine the period of this cyclicity, small scale variations in progradation rate must be determined. However, due to the limited number of available dates it is difficult to determine the exact period of this cyclicity.
End member modeling of the western beach ridge sediments shows a clear shift towards more coarse end members compared to the previous period (Fig. 12: Transect West). These coarse end members gradually increase in northward direction, which can be related to a gradual increase in sediment supply of the (secondary) Grijalva channel belt. This phase of delta evolution can be directly correlated with sedimentary zone 3 and dating of cores 179 (west) and 336 (east) puts this phase between 1700 BC and 100 BC.

Phase 4 *Age: 100BC – 1250AD*

Phase 4 covers the period ranging from 100 BC to 1150 AD and can be correlated with sedimentary zone 5 and part of zone 6. During this phase of delta progradation continues in both the eastern and western part of the delta. End member modeling along transect A shows that from roughly 400 AD (core 426), the contribution of finer end members (EM3-EM4) starts to increase. This reflects the gradual increase in the contribution of Usumacinta sediments. However, from 1000 AD (core 380) the contribution of these finer end-members decreases significantly. This pin-points the shift in sediment supply of the Usumacinta towards the west and marks the period from which the Usumacinta started to bifurcate and merge with the (secondary) Grijalva channel belt in the southern part of the delta (Fig. 18). Eventually leading to the Usumacinta delta lobe in the east changing from an aggrading towards an eroding coastline.
Around 350 AD, a relatively high set of beach ridges is formed (Fig. 18). Beach ridge morphology shows no evidence of erosion during this phase; however magnetic susceptibility values along these ridges are, especially for the eastern cores, relatively high. As no evidence exists for large scale erosion, this increase in magnetic susceptibility values can possibly be related to volcanic activity in the Grijalva drainage basin. The resulting pulse of magnetite would be transported towards the delta by the Grijalva, explaining why these increased magnetic susceptibility values are best observed in the eastern part of the delta. Dating of cores 393 and 426/179 puts this phase of delta evolution between 100 BC and 1250 AD.

T.G. Winkels
Faculty of Geosciences
Utrecht University
Department Physical Geography

Phase 5 *Age: 1250AD – Present*

The last phase of beach formation is characterized by 1) strong progradation around the merged channel belt of the Grijalva and Usumacinta and 2) the erosion of the old Usumacinta delta lobe. Erosion of this large coastal lobe resulted in the input of extra sediment in the system. The bulk of sediment is transport towards the east, by the dominant longshore currents, building a large group of beach ridges (Zone X). However, extra sediment also becomes available westward of the old lobe. This phase of delta evolution can be correlated to sedimentary zone X and part of zone 6 (Fig. 18).

Age models show an increase in delta progradation for both transects during this period (Fig. 17). This increase in progradation rate can possible explained by an increase in sediment supply, resulting from the erosion of the old Usumacinta delta lobe. Another possibility is the erosion of older beach ridges eroded out by the newly formed channel of the Usumacinta. However this would only partly explain the increase in delta progradation, as the eroding by this new channel does not produce enough extra sediment input.

Round 1500 AD the Grijalva shifted more in the direction of the Usumacinta causing the Rio Seco to silt up. This caused a concentration of the discharge through the main channel of the Grijalva also causing an increasing in sediment flux.

During the mid-20th century the construction of dams upstream in the Grijalva eventually resulted in decrease in the supply of coarser material; hence most recent beach ridges are composed of significantly finer sediments.

T.G. Winkels
Faculty of Geosciences
Utrecht University
Department Physical Geography

7. Discussion

Using beach ridge systems for paleo-environmental reconstruction requires consideration of valid assumptions on the genesis and associated processes (Tamura, 2012). One assumption made is that individual beach ridges develop simultaneously throughout the entire study area. When looking at the Usumacinta-Grijalva beach ridge complex it may be possible that the sedimentary signal in a single beach ridge does not reflect a single time period. Normally this does not pose a problem as most investigated beach ridge systems are relatively small (Brooke et all., 2008; Clemmensen et all., 2010; Pontee et all., 2004). However, due to the large dimension and fast progradation rate of this beach ridge complex this may pose a problem. This would lead to a wrong interpretation of transect L, which than would reflect the sedimentary changes over a longer period of time instead of over a distinct time period. In order to determine this formation processes and sediment transport rates should be investigated in more detail.

Most studies (e.g. Brooke et al.; Frihy et al., 2008; Nott et al., 2013; Otvos, 1969; Pontee et al., 2004; Martin, 1996) uses standard grain-size parameters (e.g. D_{50}) as means for representing sedimentary characteristics of beach ridge deposits. Besides these standard grain-size parameters this study uses EMM, which looks at contributions of individual sediments *populations* to represent sedimentary characteristics of beach ridge deposits. These end-members contain more information about active processes than standard grain-size parameters. For example: for the period just after the avulsion of the Usumacinta standard grain-size analysis show gradually increasing D_{50} values coinciding with a decrease in sorting/kurtosis values (Fig. 9A Transect A 378-393). Using standard grain-size parameters it is difficult to say what caused this change in sedimentary signal. With EMM this change in sedimentary signal could be linked to a change in the contribution of EM2 (Fig. 13 Transect A 378-393) which is probably the result of the changes in one individual processes or in this case provenance (erosion of the old Usumacinta delta lobe). Labeling of individual end-members may, however, pose a problem, as the individual sediments populations are the result of non-constant mixing of different process and/or provenance signals.

The genesis processes play an important role in explaining internal variations of the sedimentary parameters. Using GPR measurements an insight in internal structure of individual beach ridges can be obtained. Variations visible in the GPR profiles are not always reflected in the sedimentary characteristics (Appendix 10). GPR measurements show a relatively horizontally deposited structure, which can be interpreted as aeolian dune deposits. However, computed grain-size distributions do not show any significant changes for this section. Hence, it is important to investigate both sedimentary signals as GPR profiles in order to get a complete picture of the beach ridge building system.

T.G. Winkels
Faculty of Geosciences
Utrecht University
Department Physical Geography

8. Conclusions

The goal of this study was to reconstruct sediment supply and sediment provenance in the Usumacinta-Grijalva delta. This was done by analyzing sediments from multiple cores taken throughout the study area. Below the different sub questions posed in the introduction will be answered.

It can be concluded that individual beach ridges are characterized by a specific grain-size distributions). Over 200 analyzed samples show large scale variations in grain-size distributions. Besides the regional variance, examinations of individual cores showed the presence of, sometime large, internal variation (Fig. 12). This thesis showed that processes such as longshore and perpendicular coastal sorting may be responsible for internal sorting of individual beach ridges however more detailed study should be performed in order to quantify these processes. Using LIDAR images, the orientation and cutoffs of different beach ridges have been used to identify six different zones (Fig. 9) which represents periods during which the position and discharge (distribution) of the multiple river channels was relatively stable. Variations in sedimentary parameters supported this subdivision, with each zone having its own specific sedimentary characteristics (Appendix 7).

Additional heavy mineral analysis should be regarded as a pilot, where the applicability of heavy minerals in determining sediment provenances for the Usumacinta-Grijalva delta is examined. Preliminary results do, however, show a possible correlation between the presence of brown amphiboles and spinel minerals in Usumacinta sediments. It also may be possible to use the presence of opaque minerals or magnetite as a trace mineral for sediments originating from the Grijalva.

As standard grain-size analysis contains less information about active processes compared to end-member analysis, a four EM (drs_unmixer) model was used to unmix the two different grain-size datasets. End-member distributions were compared to reference samples of which the provenance was clear. Based on this comparison, the coarser end-members (EM1 and EM2) are to be related to the Grijalva river system, while the finer end-members (EM3 and EM4) are related to the Usumacinta river system. By analyzing EM abundance along transect changes in the relative contribution of the different river systems could be deduced. Using these contributions in combination with other sediment characteristics (standard grain-size parameters, magnetic susceptibility) five phases of delta evolution could be identified for the Usumacinta-Grijalva delta. As Usumacinta and the Grijalva are the dominant source of sediment used for beach ridge formation, changes in the relative contributions of these river systems become apparent when analyzing the sedimentary characteristics of individual beach ridges. The location of the river systems plays a key role in the evolution of the delta. Large scale changes in the location of these rivers systems, due to avulsion, are directly reflected both the orientation/location and sediment characteristics of the beach ridges. Using the different dating techniques theses phases of delta progradation were dated (Fig. 17).

T.G. Winkels
Faculty of Geosciences
Utrecht University
Department Physical Geography

9. Recommended future research

Based on the discussion and conclusions the following section poses some recommendations for future research..

Processes Although GPR measurements give an insight in the internal structure of a individual beach ridge, beach ridge formation processes remain so far unknown. Hence it beach ridge formation in the Usumacinta-Grijalva delta should be investigated on a process based scale. This could be done by e.g. monitoring of present-day aggradation beaches and by monitoring offshore bathymetry. Besides, individual beach ridge formation processes the influence of longshore and perpendicular coastal sorting processes should also be investigated.

Heavy minerals Only a few samples were examined heavy minerals, this should be viewed as a pilot, where the applicability of heavy minerals in determining sediment provenances for the Usumacinta-Grijalva delta is examined. However, the examined samples show a pattern with significantly higher percentages of opaque minerals for Usumacinta deposits. Besides examining more delta samples, the establishment of a clear Usumacinta and Grijalva reference signal is critical. Therefore, more reference samples of the Usumacinta and Grijalva should be collected and examined. Also the variability of heavy minerals along the rivers course should be investigated in order to determine whether the reference samples can indeed be used as a reference.

T.G. Winkels
Faculty of Geosciences
Utrecht University
Department Physical Geography

10. Reference list

Aitken, M.J., (1998). An Introduction to Optical Dating. Oxford University Press. London, pp267.

Anthony, E.J., (1995). Beach-ridge development and sediment supply: examples from West Africa. Marine Geology 129, p175–186.

Austin, L.G. and Shaw, I. (1983). A method for inter- conversion of Microtrac and sieve size distributions. Powder Technology 35, p271-278.

Bateman, R., Catt, J.A. (2007). Provenance and palaeoenironmental interpretation of superficial deposits, with particular reference to post-depositional modification of heavy mineral assemblages. Sedimentology 58, p151-188.

Beuselinck, L., Govers, G., Poesen, J., Degraer, G., Froyen, L. (1998). Grain-size analysis by laser diffractometry: Comparison with the sieve-pipette method. Catena 32, p193-208.

Bird, E.F.C., (1960). The formation of sand beach-ridges. Australian Journal of Science 22, p349–350.

Blott, S.J., Pye, K. (2001). Gradistat: A grain size distribution and statistics package for the analysis of unconsolidated sediments. Earth Surface Processes and Landforms 26, p1237-1248.

Bridge, J.S., (1981). Hydraulic interpretation of grain-size distributions using a physical model for bedload Transport. Journal of Sedimentary Petrology 51, p1109-1124.

Brooke, B., Ryan, D., Pietsch, T., Olley, J., Douglas, G., Packett, R., Radke, L., Flood, P., (2008). Influence of climate fluctuations and changes in catchment land use on Late Holocene and modern beach-ridge sedimentation on a tropical macrotidal coast: Keppel Bay, Queensland, Australia. Marine Geology 251, p195–208.

Cascalho, J., Fradique, C. (2007). The sources and hydraulic sorting of heavy minerals on the northen Portuguese continental margin. Sedimentology 58, p75-100.

Carter, R.W.G.,(1986). The morphodynamics of beach-ridge formation: Magilligan, Northern Ireland. Marine Geology 73, p191-214.

Clemmensen, L.B. and Nielsen, L., (2010). Internal architecture of a raised beach ridge system (Anholt, Denmark) resolved by ground-penetrating radar investigations. Sedimentary Geology 223, p281–290.

Curray, J.R., Emmel, F.J., Crampton, P.J.S. (1969). Holocene history of a strand plain, lagoonal coast, Nayarit, Mexico. Ayala-Casteñares, UN Symposium, UNAM-UNESCO, Mexico, D.F, p63–100.

Curray, J.R. (1996). Origin of beach ridges: Comment on Tanner. Origin of beach ridges and swales. Marine Geologie129, p149-161.

Davies, J.L., (1957). The importance of cut and fill in the development of sand beach ridges. Australian Journal of Science 20, p105–111.

Engelhart, S.E., Horton, B.P., Douglas, B.C., Peltier, W.R. and Törnqvist, T.E., (2009). Spatial variability of late Holocene and 20th century sea-level rise along the Atlantic coast of the United States. Geology 37, p1115–1118.

Espíndola, J.M., Macías, J.L., Tilling, R.I., Sheridan, M.F., (2000).Volcanic history of El Chichon Volcano (Chiapas, Mexico) during the Holocene, and its impact on human activity. Bulletin of Volcanology 62, p90-104.

Feniak, M.W., (1944). Grain sizes and shapes of various in igneous rocks. American Mineralogist 29, p415-421.

Folk R.L., Ward W.C. (1957). Brazos River bar: a study in the significance of grain size parameters. Journal of Sedimentary Petrology 27,p3–26.

Frihy, O. E., S. M. Shereet & M. M. El Banna (2008): Pattern of Beach Erosin and Scour Depth along the Rosetta Promontory and their Effect on the Existing Protection Works, Nile Delta, Egypt. Journal of Coastal Research 24, p857-866.

Galloway, W. E., (1975). Process framework for describing the morphologic and stratigraphic evolution of deltaic depositional systems, in Broussard. Deltas: Houston Geological Society, p87–98.

T.G. Winkels
Faculty of Geosciences
Utrecht University
Department Physical Geography

Garzanti, E. Ando, S. (2007). Heavy mineral concentration in modern sands: implications for provenance interpretation. Sedimentology 58, p517-545

Gee, G.W., Bauder, J.W., (1986). Particle-size analysis. In: Klute, A. (Ed.), Methods of Soil Analysis: Part 1. Physical and Mineralogical Methods, 2nd edn., Agronomy, 9. Soil Science Society of America, Madison, USA, pp. 383–411.

Gischlera, E., Harold Hudsonb, J. (2004). Holocene development of the Belize Barrier Reef. Sedimentary Geology 164, p223 – 236.

Hoekstra, P., Houwman, K.T. (1997). Selective Sediment Transport in the Nearshore Zone: Field observations and Potential Mechanisms. Coastal Dynamics 97, p78-87.

Hail, J.H.R. (1969).The origin and development of the Umina-Woy Woy beach-ridge system, Broken Bay. The Australian Geographer11, p1–12.

Heslop. D. and Dillon. M. (2007). Unmixing magnetic remanence curves without a priori knowledge. Geophysical Journal International170, p556-566.

Hine, A.L., (1979). Mechanism of berm development and resulting beach growth along a barrier spit complex. Sedimentology 26, p333–351.

Jonasz, M. (1991). Size, shape, composition and structure of microparticles from light scattering. In: Principles, methods and applications of particle size analysis. Cambridge University Press, p143-162.

Komar, P.D., (1998). Beach Processes and Sedimentation, 2nd edition. Prentice Hall, NewJersey. 544 pp.

Komar, P.D.,(2007). The entrainment, transport and sorting of heavy minerals by waves and currents. Developments in Sedimentology 58, p3-48.

Konert, M., Vandenberghe, J. (1997). Comparison of laser grain size analysis with pipette and sieve analysis: a solution for the underestimation of the clay fraction. Sedimentology 44, p523-535.

Kretz, R., (1966). Grain-size distrubutions for certain metamorphic minerlas in relation to nucleation and growth. Journal of Geology 74, p147-173.

Mange, M.A., Maurer, H.F.W., (1992). Heavy Minerals in Colour. Chapman and Hall, London, p147.

Martin, L., Suguio, K., Flexor, J.M., Dominguez, J.M.L., Bittencourt, A.C.S.P. (1996). Quaternary Sea-level History and Variation in Dynamics along the Central Brazilian Coast: Consequences on Coastal Plain Construction. Anais da Academia Brasileira de Ciencias 68, p300-325.

Middelton, G.V., (1976). Hydraulic interpretation of sand size distributions. Journal of Geology 84, p405-426.

Morton, A.C., Hallsworth, C. (2007). Stability of detrital heavy minerals during burial diagenesis. Developments in Sedimentology 58, p215-245.

NEN 5753 (1990). Bepaling van de korrelgrootteverdeling met behulp van zeef en pipet. Nederlands, Normalisatie-instituut, Delft.

Nooren, C.A.M, Hoek, W.Z, Tebbens, L.A, Martin Del Pozzo, A.L., (2009). Tephrochronological evidence for the late Holocene eruption history of El Chichón Volcano, Mexico. Geofisica Internacional 48, p97-112.

Nott, J., Smithers, S., Walsh, K. and Rhodes, E., (2009). Sand beach ridges record 6000 year history of extreme tropical cyclone activity in northeastern Australia. Quaternary Science Reviews 28, p1511–1520.

Nott, J., Chague-Goff, C., Goff, J., Sloss, C., Riggs. N. (2013). Anatomy of sand beach ridges: Evidence from severe Tropical Cyclone Yasi and its predecessors, northeast Queensland, Australia. Journal of Geophysical Research 118, p1710-1719.

Otvos, E.G. (1969). A subrecent beach ridge complex in Southeastern Louisiana. Bulletin of the Geological Society of America 80, p2353-2358.

Pohl, M.E.D., Piperno, D.R., Pope, K.O. and Jones, J.G., (2007). Microfossil evidence for pre-Columbian maize dispersals in the neotropics from San Andrés, Tabasco, Mexico. PNAS 104, p6870-6875.

Pontee, N.I., Pye, K. , Blott, S.J. (2004). Morphodynamic behaviour and sedimentary variation of mixed sand and gravel beaches, Suffolk, UK. Journal of Coastal Research 20, p256-276.

T.G. Winkels
Faculty of Geosciences
Utrecht University
Department Physical Geography

Pope, K.O., Pohl, M.E.D., Jones, J.G., Lentz, D.L., Von Nagy, C., Vega, F.J. and Quitmyer, I.R., (2001). Origin and Environmental Setting of Ancient Agriculture in the Lowlands of Mesoamerica. Science 292, p1370-1373.

Prins, M.A., (1999). Pelagic, hemipelagic and turbidite deposition in the Arabian Sea during the late Quaternary: Unravelling the signals of aeolian and fluvial sediment supply as functions of tectonics, sea-level and climate change by means of end-member modelling of siliciclastic grain-size distributions (Ph.D. thesis). Geologica Ultraiectina 168, p192.

Prins, M.A. and Weltje, G. J., (1999). End-member modeling of siliciclastic grain-size distributions: The late Quaternary record of aeolian and fluvial sediment supply to the Arabian Sea and its paleoclimatic significance, in Harbaugh, J., et al., eds., Numerical experiments in stratigraphy: Recent advances in stratigraphic and sedimentologic computer simulations, Society for Sedimentary Geology 62, p91-111.

Psuty, N.P., 1967, The Geomorphology of Beach-ridges in Tabasco,Mexico. Louisiana State University Press, p51.

Rhodes, E.G., Polach, H.A., Thom, B.G., Wilson, S.R., (1980). Age structure of Holocene coastal sediments, Gulf of Carpentaria, Australia. Radiocarbon 22, p718–727.

Shillabeer, N., Hart, B. and Riddle, A.M. (1992). The use of a mathematical model to compare particle size data derived by dry sieving and laser analysis. Estuarine, Coastal and Shelf Science 35, p105-111.

Stapor, F.W., (1975). Holocene beach-ridge plain development, northwest Florida. Zeitschrift für Geomorphologie supply. Bd. 22, p116–144.

Shukla, S.B., Chowksey, V.M., Prizomwala, S.P., Ukey, V.M., Bhatt, N.P., Maurya, D.M. (2013). Internal sedimentary architecture and coastal dynamics as revealed by ground penetrating radar, Kachchh coast, western India. Acta Geophysica 61, p1196-1210.

Tanner, W.F., (1995). Origin of beach ridges and swales. Marine Geology 129, p149–161.

Tamura, T., Murakami, F., Nanayama, F., Watanabe, K. and Saito, Y., (2008). Ground-penetrating radar profiles of Holocene raised-beach deposits in the Kujukuri strand plain, Pacific coast of eastern Japan. Marine Geology 248, p11–27.

Taylor, M.J. & Stone, G.W. (1996). Beach-ridges: A review. Journal of Coastal Research 12, p612-621.

van Loon, A.J., Mange, M. (2007). In situ dissolution of heavy minerals through extreme weathering, and the application of the surviving assemblages and their dissolution characteristics to correlation of Dutch and German silver sands. Sedimentology 58, p189–213.

van der Plicht, J, Wijma, S., Aerts, A.T., Pertuisot, M.H., Meijer, H.A.J. (2000). Status report: The Groningen AMS facility. Radiocarbon 172, p58-65.

Wallinga, J. (2002). Optically stimulated luminescence dating of fluvial deposits: a review. Boreas 31, p303-322

Weltje, G.J. (1997). End-Member modeling of compositional data. Numerical-statistical algorithms for solving the explicit mixing problem. Mathematical Geology 29, p503-549.

T.G. Winkels
Faculty of Geosciences
Utrecht University
Department Physical Geography

A

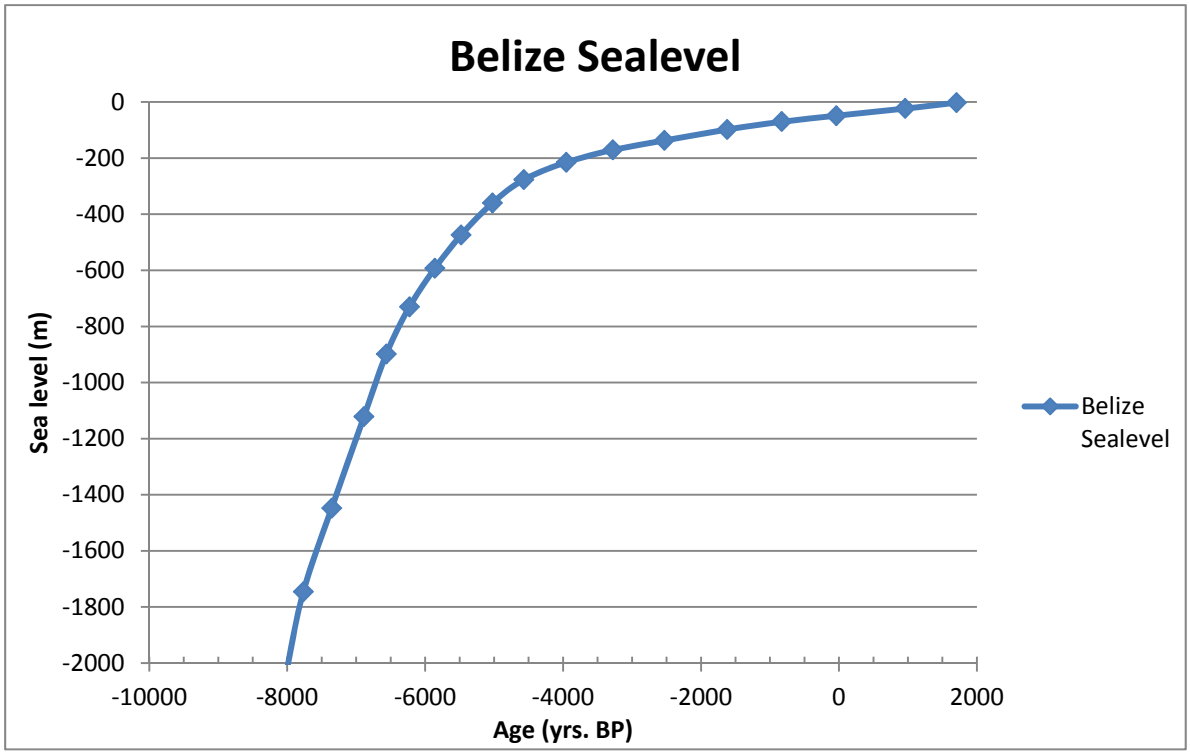

Sea level curve constructed for Belize according to Gischlera et al. (2004)

B

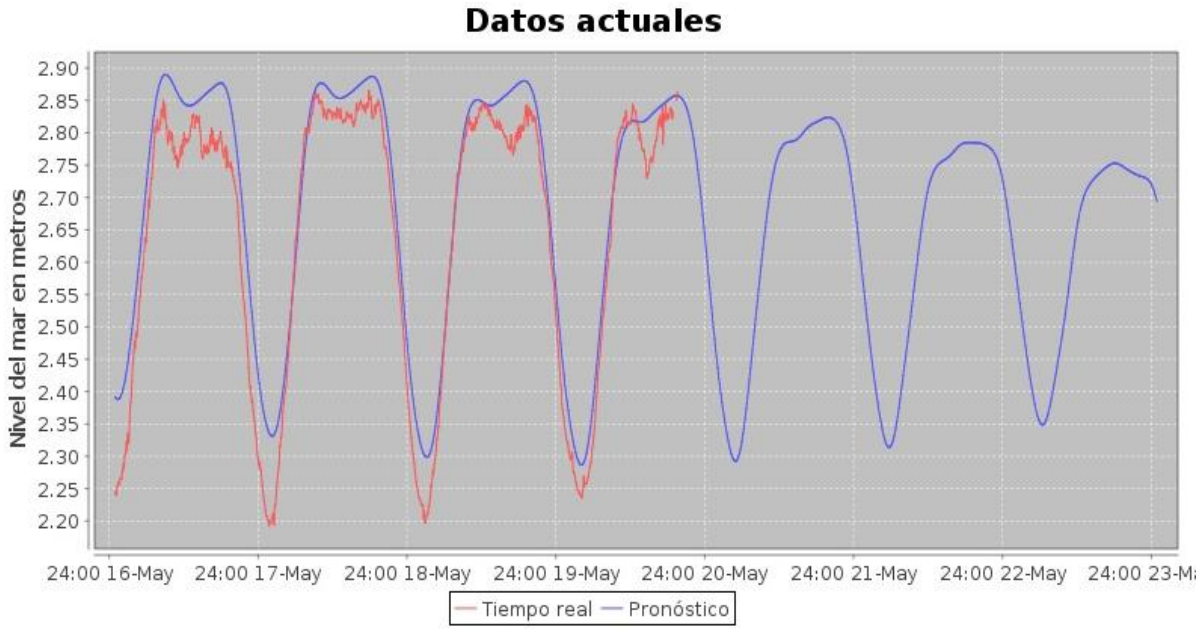

Tidal amplitude (spring tide), with in blue to projected tide and in red the measured tide at the tide gauge in Ciudad del Carmen.

Appendix 2 GPR Measurements

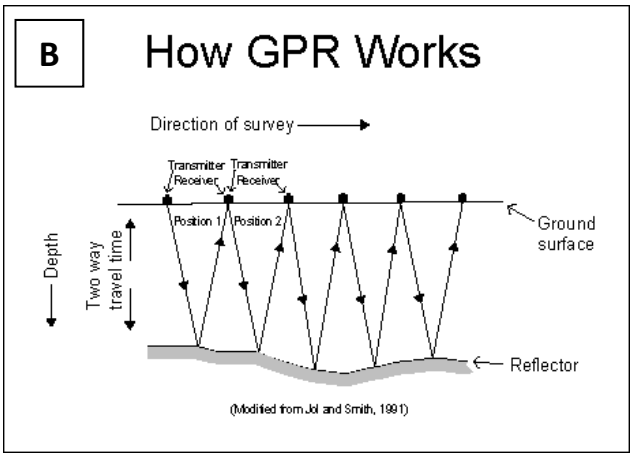

A: GPR measurements preformed during the field campaign of 2012 (Photo: W.Z Hoek) and B: the basic principle behind the GPR method. C: the transect along with the GPR measurements were obtained and the multiple analyzing steps which were performed by R. van Dam

All GPR analyzing was done by R. van Dam.

A few notes:

- GPS coordinates for Flag 277 and Core 196 are nearly identical
- Waypoints 276, 277 and 279 are each 30m apart.
- Waypoint 279 is last in the GPR field notes, but the distance between 278 and 279 is likely a bit more than 30 m.

To improve the visual quality of the data, various processing steps have been employed. These steps included:

• A time *shift* to remove negative times from the data ('move starttime')
• A time *cut* to remove data without signal (below ~70ns two-way-traveltime)
• A 'dewow' to remove low frequency instrument noise
• A frequency filter (bandpass butterworth 50-300 MHz) to emphasize relevant frequency content
• A gain to amplify deeper signals (cutting off at a maximum value to not allow noise at depth to be amplified too much)
• Topographic correction obtained from the lidar data

Appendix 3 Sieving Analysis

A

Sieve 12	500µm
Sieve 11	300µm
Sieve 10	250µm
Sieve 9	200µm
Sieve 8	212µm
Sieve 7	180µm
Sieve 6	150µm
Sieve 5	125µm
Sieve 4	106µm
Sieve 3	90µm
Sieve 2	75µm
Sieve 1	53µm

B

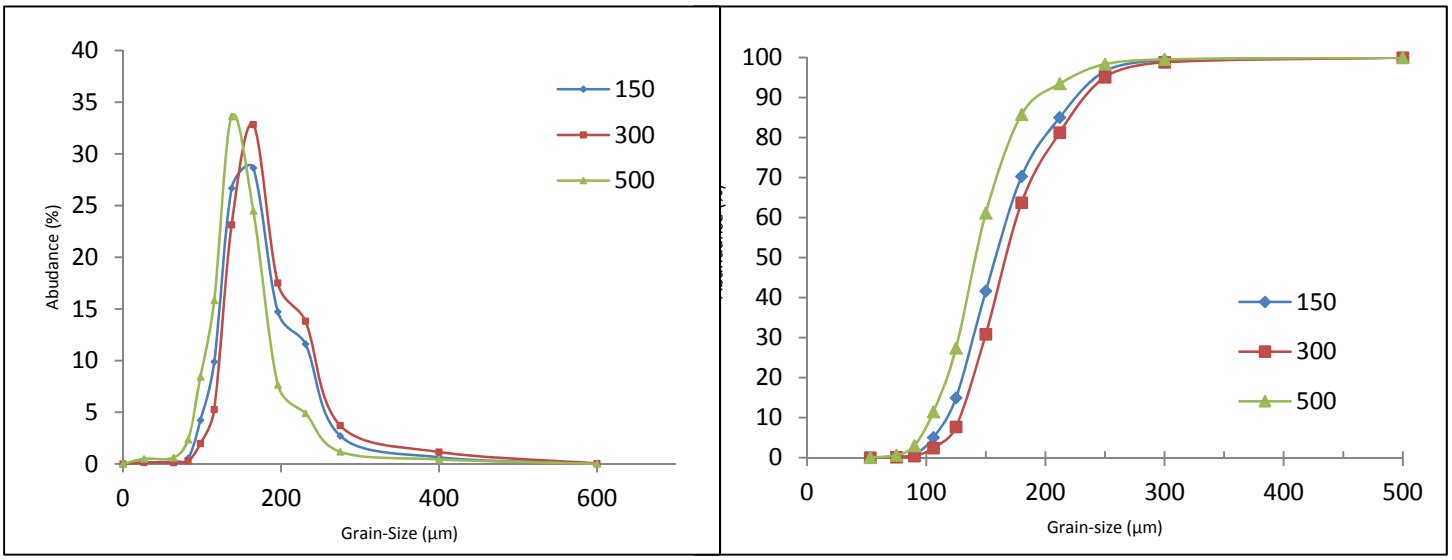

Example of grain-size distributions and cumulative distribution for core 387

Appendix 4 End-Member correction

Individual End-Member distributions:

Wavelength	*26*	*53*	*75*	*90*	*106*	*125*	*150*	*180*	*212*	*250*	*300*	*500*	Sum	"Correction factor"
EM1	0	0	0.189119	2.254921	1.205025	0	0	6.36147	24.29826	28.22067	38.89605	1.7114259	103.14	1.03
EM2	1.626905	1.165238	0.79082	0.117993	0	5.413574	31.11127	25.50748	27.54367	8.305518	0	0	101.58	1.02
EM3	0	0	0	0	6.985591	41.57793	36.78816	11.72549	4.91876	0	0	0	102.00	1.02
EM4	1.578829	1.6487	4.321176	18.23761	26.8752	34.39199	9.670961	0	0	0.618981	2.344213	0.1085096	99.80	1.00

Corrected_EM = Original_value*(1/Correction_factor)

Correction_factor = Sum/100

	26	*53*	*75*	*90*	*106*	*125*	*150*	*180*	*212*	*250*	*300*	*500*	
'corrected' EM1'	0	0	0.183367	2.186337	1.168374	0	0	6.167984	23.55922	27.36233	37.71301	1.6593722	100.00
'corrected' EM2'	1.601561	1.147085	0.7785	0.116155	0	5.32924	30.62662	25.11012	27.11459	8.176133	0	0	100.00
'corrected' EM3'	0	0	0	0	6.848892	40.76431	36.06826	11.49604	4.822506	0	0	0	100.00
'corrected' EM4'	1.582054	1.652067	4.330002	18.27486	26.9301	34.46223	9.690713	0	0	0.620245	2.349001	0.1087312	100.00

End-Member Abundances:

Sample#		EM1	EM2	EM3	EM4
378	*150*	0.123528	0.060106	0.333692	0.482673
383	*150*	0.003697	0.752389	0.201968	0.041947
387	*150*	0.017393	0.29085	0.507307	0.184449
393	*150*	0	0.540129	0.337662	0.122209
394	*150*	0.048374	0.08973	0.435375	0.426521
398	*150*	0.201289	0.504651	0.134597	0.159463
409	*150*	0.037892	0.368475	0.46418	0.129453

EM1	**EM2**	**EM3**	**EM4**	**Sum**
0.127403	0.061057	0.340353	0.481689	1.01
0.003812	0.764295	0.205999	0.041861	1.02
0.017938	0.295453	0.517433	0.184073	1.01
0	0.548676	0.344401	0.12196	1.02
0.049892	0.09115	0.444064	0.425652	1.01
0.207604	0.512637	0.137283	0.159138	1.02
0.03908	0.374306	0.473445	0.129189	1.02

EM = Original_value*Correction_factor

EM1	**EM2**	**EM3**	**EM4**	**Sum**
0.1260792	0.06	0.33682	0.476682758	1.00
0.0037526	0.752	0.20276	0.041203173	1.00
0.0176751	0.291	0.50984	0.181371405	1.00
0	0.541	0.3393	0.120153376	1.00
0.0493608	0.09	0.43934	0.421121765	1.00
0.2042014	0.504	0.13503	0.156529649	1.00
0.0384641	0.368	0.46598	0.127151777	1.00
0.03618	0	0.46631	0.497510499	1.00

Corrected_EM_Abudance = Original_value*(1/Sum (e.g. 1.01))

Appendix 5 Sea level correction

Assuming that present-day ground water table are match present day sea level. Paleo water tables are constructed using the sea level curve of Belize.

Core	Groundwater Level (cm-mv)	± Distance from shore (m)	Expected age (cal. yr AD)	Correction (cm)	Corrected * Groundwater Level (cm-mv)	Heavy Mineral Depth (cm-mv)	Sample depth (cm-mv)
375	140	-4651	813	-27	113	263	250
376	120	-4571	835	-26	94	244	250
377	100	-4463	865	-26	74	224	200
378	100	-4343	898	-25	75	225	250
379	120	-4242	926	-24	96	246	200
380	130	-4152	951	-24	106	256	250
381	160	-4055	977	-23	137	287	300
382	160	-3950	1006	-23	137	287	300
383	120	-3844	1036	-22	98	248	250
384	130	-3736	1065	-21	109	259	250
385	140	-3639	1092	-21	119	269	250
386	150	-3527	1123	-20	130	280	300
387	130	-3417	1153	-19	111	261	250
388	120	-3387	1162	-19	101	251	250
389	120	-3357	1170	-19	101	251	250
390	130	-3247	1200	-18	112	262	250
391	160	-3134	1231	-18	142	292	300
392	130	-3058	1252	-17	113	263	250
393	250	-3037	1258	-17	233	383	400
394	120	-4981	749	-28	92	242	250
395	110	-5124	699	-29	81	231	250
396	110	-5223	664	-30	80	230	250
397	150	-5313	632	-30	120	270	300
398	130	-5429	591	-31	99	249	250
399	110	-5484	572	-32	78	228	250
400	110	-5596	533	-32	78	228	250
401	120	-5743	481	-34	86	236	250
409	120	-5223	664	-30	90	240	250
411	90	-5223	664	-30	60	210	200
413	100	-5313	632	-30	70	220	200
414	100	-5429	591	-31	69	219	200
416	150	-5428	592	-31	119	269	250
426	130	-5843	446	-34	96	246	250
427	240	-5519	560	-32	208	358	350
428	110	-652	2271	0	110	260	250
429	160	-1964	1810	0	160	310	300
430	60	-1180	2086	0	60	210	200
432	100	-7770	-232	-52	48	198	200

*Distances towards the coast were measured perpendicular to the beach ridges using Geographic information system (GIS) and the LIDAR images ((INEGI, 2008)

*Sea level curve of Belize was used (Gischlera et al., 2004)

*Assuming the minimum groundwater level corresponds with sea level.

Appendix 6 Chronology

A OSL dates

OSL Samples

NCL	Client	X	Y	Depth (m)	Equivalent dos (GY)	Dos rate (GY/ka)
NCL-411227	East transect 112 ridge	18_35_42.9	92_35_37.3	2.05	1.75 ± 0.13	2.21 ± 0.10
NCL-411228	West transect 179 dune	18_27_07.7	92_47_34.1	0.725	2.87 ± 0.29	2.72 ± 0.1
NCL-411229	East transect 252 ridge	15_35_30.3	92_34_30.3	2.075	4.85 ± 0.51	2.34 ± 0.1

NCL	Client	X	Y	Depth (m)	Age (ka)	Age (AD)
NCL-411227	East transect 112 ridge	18_35_42.9	92_35_37.3	2.05	0.79 ± 0.07	1218 ± 66
NCL-411228	West transect 179 dune	18_27_07.7	92_47_34.1	0.725	1.05 ± 0.11	955 ± 113
NCL-411229	East transect 252 ridge	15_35_30.3	92_34_30.3	2.075	2.08 ± 0.24	±

B C^{14} dates

Transect	Sample	GrA	Age BP	Calibrated age (yr AD) 95.4% probability	68.20% probability	%C	d13C	delta13 AMS
A	379-280L	58030	1015 ± 35	1028 ± 124	1010.5 ± 25.5	48.16	-28.29	
A	389-330L	58031	900 ± 40	1124.5 ± 90.5	1116.5 ± 71.5	52.21	-30.48	
A	393-300L	58032	715 ± 35	1305 ± 81	1278.5 ± 16.5	45.26	-30.25	
A	397-350L	58033	1390 ± 35	637.5 ± 44.5	642.5 ± 21.5	54.93	-30.06	
A	426-255L	58034	1690 ± 40	336 ± 86	332 ± 70	52.56	-29.75	
A	426-885L	58035	1665 ± 35	393 ± 137	379.5 ± 35.5	45.92	-29.92	
A	429-250L	58037	300 ± 35	1572 ± 88	1583.5 ± 62.5	49.78	-27.39	
B	432-300L	58144	3880 ± 40	-2340 ± 130	-2378 ± 78	51.86	-30.65	
B	**438-170L**	58039	3005 ± 35	-1255 ± 131	-1251 ± 117	52.59	-29.64	
B	**440-350L**	58040	2125 ± 40	-199 ± 155	-131.5 ± 70.5	50.59	-29.82	
B	443-230L	58041	165 ± 35	1787 ± 126	1795 ± 127	50.18	-28.11	
B	444-150L	58042	350 ± 35	1546 ± 90	1554 ± 76	49.99	-28.64	
B	446-275L	58043	1060 ± 40	960 ± 68	962 ± 58	52.03	-29.53	
C	469-160L	58044	1210 ± 35	813.5 ± 124.5	824 ± 54	49.70	-29.63	
C	469-325L	58048	1360 ± 35	687 ± 77	661.5 ± 19.5	46.92	-29.51	
A	193-171L	55022	1250 ± 30	773 ± 97	730 ± 44	61.50	-30.05	-31.4
A	196-204L	55023	1235 ± 30	783 ± 97	778 ± 84	61.50	-30.94	-31.67
A	252-485L	55021	2420 ± 35	-575.5 ± 174.5	-555 ± 147	55.10	-31.42	-32.62
A	336-368L	54940	3410 ± 45	-1746 ± 132	-1696.5 ± 58.5	38.70	-29.70	
B	185-471L	55029	2665 ± 35	-846 ± 50	-820 ± 22	42.30	51.60	-30.49
B	188-310L	55020	3930 ± 35	-2430 ± 131	-2411.5 ± 64.5		-30.33	-31.29

Oxcal 4.2 (IntCal 13 Calibration curve)

Transect	SampleName	GrA	range at 95.4% prob.	range at 68.2% prob.
A	379-280L	58030	904 - 1152	985 - 1036
A	389-330L	58031	1034 - 1215	1045 - 1188
A	393-300L	58032	1224 - 1386	1262 - 1295
A	397-350L	58033	593 - 682	621 - 664
A	426-255L	58034	250 - 422	262 - 402
A	426-885L	58035	256 - 530	344 - 415
A	429-250L	58037	1484 - 1660	1521 - 1646
B	432-300L	58144	-2470 - -2210	-2456 - -2300
B	**438-170L**	58039	-1386 - -1124	-1368 - -1134
B	**440-350L**	58040	-354 - -44	-202 - -61
B	443-230L	58041	1661 - 1913	1668 - 1922
B	444-150L	58042	1456 - 1636	1478 - 1630
B	446-275L	58043	892 - 1028	904 - 1020
C	469-160L	58044	689 - 938	770 - 878
C	469-325L	58048	610 - 764	642 - 681
A	193-171L	55022	676 - 870	686 - 774
A	196-204L	55023	686 - 880	694 - 862
A	252-485L	55021	-750 - -401	-702 - -408
A	336-368L	54940	-1878 - -1614	-1755 - -1638
B	185-471L	55029	-896 - -796	-842 - -798
B	188-310L	55020	-2561 - -2299	-2476 - -2347

Zone 1

Core (nmbr)	Depth (cm-mv)	GS (µm)	Mag.Sus	
306	60	-	0.20	*2012*
	70	-	0.20	*2012*
	100	-	0.27	*2012*
303	50	-	0.09	*2012*
124	95	195	0.16	*2012*
144	105	250	0.27	*2012*
307	420	220	-	*2012*
308	1000	-	0.29	*2012*

Zone 2

Core (nmbr)	Depth (cm-mv)	GS (µm)	Mag.Sus	Sorting	Kurtosis	
148	71.5	154	0.04	-	-	*2012*
453	150	244	0.73	1.485	1.801	*2013*
452	150	169	0.135	1.296	1.204	*2013*
449	150	179	0.30	1.325	1.140	*2013*
451	130	-	0.17	-	-	*2013*
	175	-	0.13	-	-	*2013*
	200	-	0.12	-	-	*2013*
192	120	164	0.75	-	-	*2012*
	135	189	2.59	1.366	1.172	*2012*
	200	216	0.33	-	-	*2012*
453	300	226	13.50	1.475	1.172	*2013*
452	300	212	0.331	1.246	0.982	*2013*
449	300	188	3.71	1.350	1.104	*2013*
451	260	-	0.18	-	-	*2013*
192	300	211	0.66	1.455	0.924	*2012*
453	500	295	0.51	1.360	0.869	*2013*
452	500	214	0.28	1.408	1.091	*2013*
449	500	239	0.26	1.436	1.161	*2013*
192	440	210	0.31	1.413	0.951	*2012*
	540	188	0.78	-	-	*2012*

Zone 3

Core (nmbr)	Depth (cm-mv)	GS (µm)	Mag.Sus	Sorting	Kurtosis	
432	150	141	0.73	1.274	1.219	*2013*
433	150	141	0.14	1.318	1.288	*2013*
188	140	155	0.91	1.312	1.280	*2012*
432	300	138	0.51	1.389	1.481	*2013*
433	300	143	0.36	1.272	1.255	*2013*
188	280	180	0.35		0.849	*2012*
432	500	134	0.53	1.236	1.194	*2013*
433	500	126	0.48	1.419	1.832	*2013*

Zone 4

Core (nmbr)	Depth (cm-mv)	GS (µm)	Mag.Sus	Sorting	Kurtosis	
434	150	0	0.23	1.313	1.099	*2013*
435	150	158	1.40	1.266	1.129	*2013*
437	150	152	0.09	1.234	1.187	*2013*
436	150	161	0.12	1.373	1.201	*2013*
438	150	-	0.78	-	-	*2013*
439	150	169	1.48	1.267	1.077	*2013*
440	150	169	2.61	1.257	1.007	*2013*
186	160	0	2.89	1.307	1.267	*2012*
434	300	0	0.41	1.322	1.119	*2013*
435	300	163	0.69	1.294	1.033	*2013*
437	300	169	0.09	1.293	0.979	*2013*
436	300	157	0.40	1.226	1.116	*2013*
438	300	-	1.02	-	-	*2013*
439	300	194	2.18	1.272	0.934	*2013*
440	300	188	0.26	1.264	0.915	*2013*
186	250	252	0.24	1.400	0.975	*2012*
434	500	0	0.31	1.434	1.105	*2013*
435	500	164	0.72	1.395	1.220	*2013*
437	500	160	0.49	1.367	1.307	*2013*
436	500	186	0.37	1.291	1.004	*2013*
438	500	-	0.63	-	-	*2013*
439	500	175	0.37	1.286	0.983	*2013*
440	500	199	0.50	1.465	1.080	*2013*
186	450	0	0.59	1.380	0.912	*2012*

Zone 5

Core (nmbr)	Depth (cm-mv)	GS (µm)	Mag.Sus	Sorting	Kurtosis	
Far West of main river channel						
462	150	149	0.93	1.276	0.914	*2013*
461	150	189	42.45	1.406	1.074	*2013*
447	150	155	3.13	1.227	1.179	*2013*
446	150	160	0.38	1.250	1.068	*2013*
445	150	160	0.34	1.236	1.233	*2013*
462	300	216	0.82	1.270	0.933	*2013*
461	300	199	0.30	0.257	0.962	*2013*
447	300	155	0.31	1.294	1.426	*2013*
446	300	151	0.53	1.322	1.322	*2013*
445	300	151	0.43	1.443	1.345	*2013*
447	500	171	0.46	1.437	1.293	*2013*
446	500	149	0.66	1.273	1.324	*2013*
445	500	149	0.61	1.320	1.485	*2013*

Core (nmbr)	Depth (cm-mv)	GS (µm)	Mag.Sus	Sorting	Kurtosis	
East of main river channel						
398	150	189	0.29	1.482	1.1	*2013*
394	150	143	0.34	1.324	1.282	*2013*
378	150	142	0.19	1.406	1.009	*2013*
383	150	179	0.14	1.275	1.016	*2013*
387	150	159	0.34	1.289	0.983	*2013*
393	150	166		1.278	1.055	*2013*
398	300	147	0.38	1.240	1.268	*2013*
394	300	142	0.43	1.368	1.322	*2013*
378	300	140	0.27	1.348	1.090	*2013*
383	300	164	0.42	1.314	0.949	*2013*
387	300	167	0.27	1.277	0.966	*2013*
393	300	200		1.272	0.928	*2013*
398	500	148	0.39	1.430	1.673	*2013*
394	500	143	0.37	1.284	1.299	*2013*
378	500	123	0.22	1.274	1.187	*2013*
383	500	141	0.21	1.334	1.200	*2013*
387	500	142	0.29	1.283	1.154	*2013*
393	500	183		1.305	0.923	*2013*

Zone 6

Core (nmbr)	Depth (cm-mv)	GS (µm)	Mag.Sus	Sorting	Kurtosis	
West of main river channel						
444	150	139	0.44	1.328	1.142	*2013*
443	150	158	4.32	1.297	1.213	*2013*
444	300	135	0.51	1.276	1.195	*2013*
443	300	164	0.57	1.289	1.017	*2013*
444	500	135	0.59	1.220	1.135	*2013*
443	500	142	1.28	1.280	1.307	*2013*

Core (nmbr)	Depth (cm-mv)	GS (µm)	Mag.Sus	Sorting	Kurtosis	
East of main river channel						
429	150	151	0.95	1.281	1.216	*2013*
428	150	219	0.28	1.756	0.695	*2013*
430	150	154	0.67	1.330	1.157	*2013*
429	300	164	0.23	1.312	1.023	*2013*
428	300	113	0.47	1.401	1.226	*2013*
430	300	135	0.57	1.251	1.225	*2013*
429	500	126	0.35	1.338	1.148	*2013*
428	450	-	0.47	-	-	*2013*

(e) Geometric (modified) Folk and Ward (1957) graphical measures

Mean	Standard deviation
$M_G = \exp \frac{\ln P_{16} + \ln P_{50} + \ln P_{84}}{3}$	$\sigma_G = \exp\left(\frac{\ln P_{16} - \ln P_{84}}{4} + \frac{\ln P_5 - \ln P_{95}}{6{\cdot}6}\right)$
Skewness	**Kurtosis**
$Sk_G = \frac{\ln P_{16} + \ln P_{84} - 2(\ln P_{50})}{2(\ln P_{84} - \ln P_{16})} + \frac{\ln P_5 + \ln P_{95} - 2(\ln P_{50})}{2(\ln P_{25} - \ln P_5)}$	$K_G = \frac{\ln P_5 - \ln P_{95}}{2{\cdot}44(\ln P_{25} - \ln P_{75})}$

Sorting (σ_G)		Skewness (Sk_G)		Kurtosis (K_G)	
Very well sorted	<1·27	Very fine skewed	$^{-}$0·3 to $^{-}$1·0	Very platykurtic	<0·67
Well sorted	1·27–1·41	Fine skewed	$^{-}$0·1 to $^{-}$0·3	Platykurtic	0·67–0·90
Moderately well sorted	1·41–1·62	Symmetrical	$^{-}$0·1 to $^{+}$0·1	Mesokurtic	0·90–1·11
Moderately sorted	1·62–2·00	Coarse skewed	$^{+}$0·1 to $^{+}$0·3	Leptokurtic	1·11–1·50
Poorly sorted	2·00–4·00	Very coarse skewed	$^{+}$0·3 to $^{+}$1·0	Very leptokurtic	1·50–3·00
Very poorly sorted	4·00–16·00			Extremely leptokurtic	>3·00
Extremely poorly sorted	>16·00				

Folk and Ward method was used to calculated the Sorting and kurtosis values (modified after Blott et al., 2001)

Appendix 8 End-members

Sieve dataset End-members

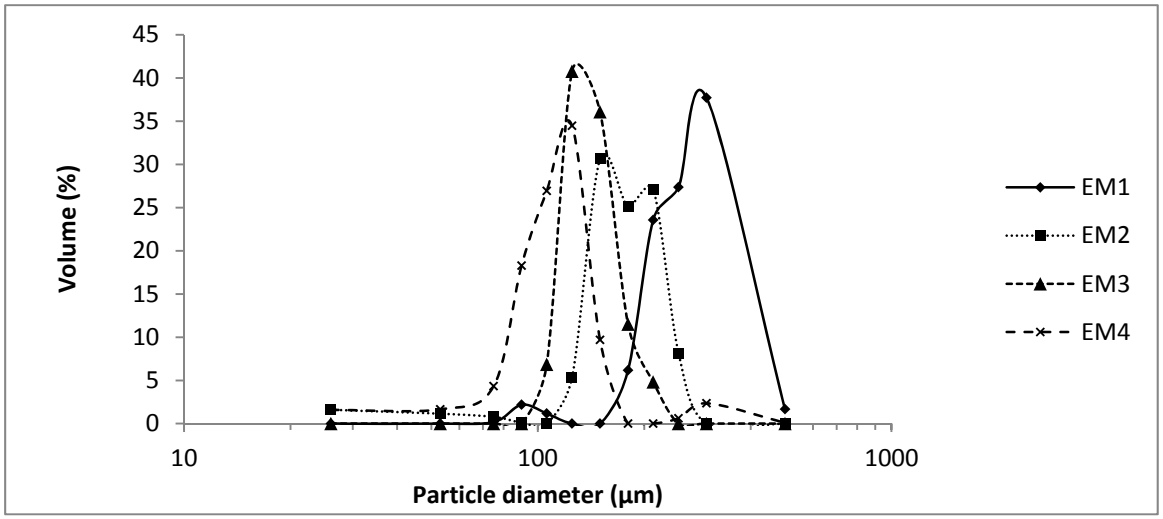

		EM1	EM2	EM3	EM4
FOLK AND	MEAN	294.3	193.9	152.9	121.4
WARD METHOD	SORTING	1.346	1.227	1.183	1.232
(µm)	KURTOSIS	0.884	0.887	0.976	1.020

Laser dataset End-members

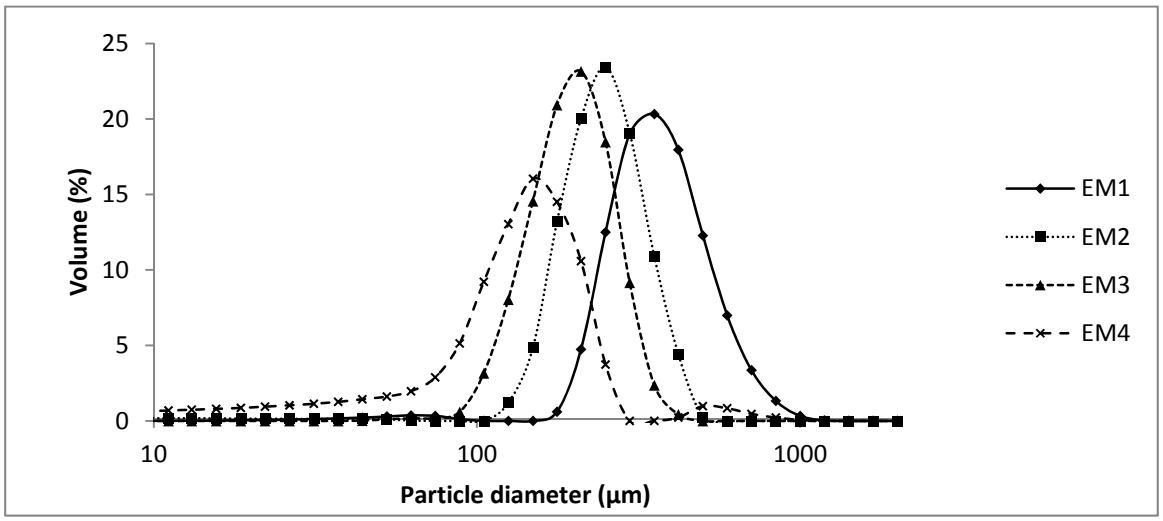

		EM1	EM2	EM3	EM4
FOLK AND	MEAN	396.0	260.9	212.2	123.2
WARD METHOD	SORTING	1.406	1.369	1.349	2.320
(µm)	KURTOSIS	0.998	1.058	0.978	2.044

Appendix 9 Heavy minerals

Counted Heavy minerals

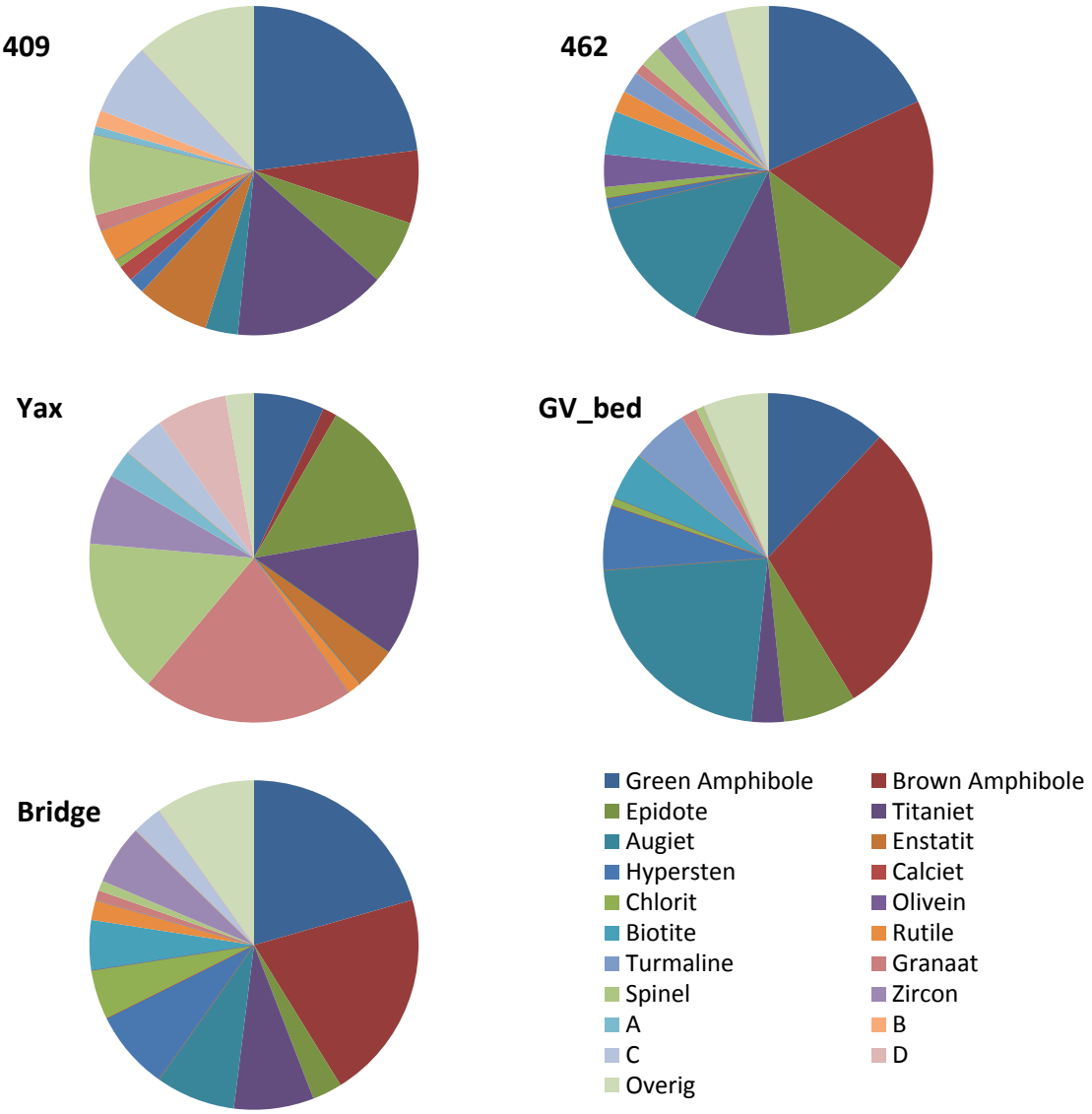

Appendix 10 GPR versus Sediments

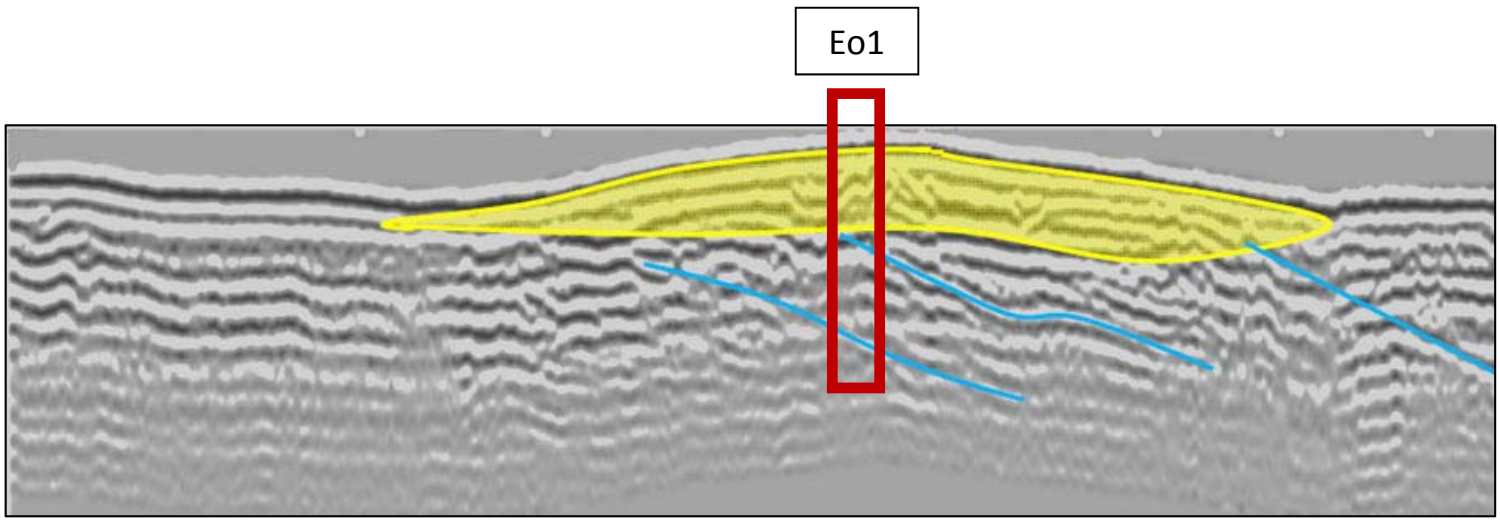

In Yellow: the relative horizontal structure, which can be interpreted as aeolian dune deposits and in Blue: a few clear dipping reflector layers.

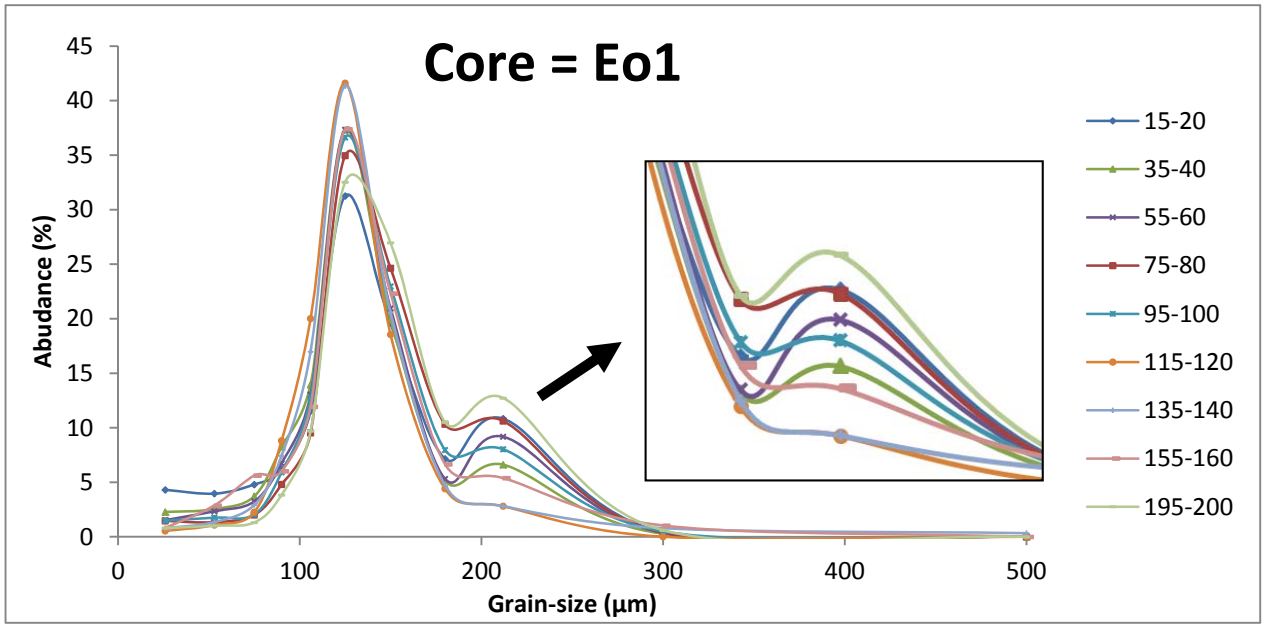

No significant difference visible